Vol. 03 No. 04 2025

RiESTech

JOURNAL
RECENT IN ENGINEERING SCIENCE AND TECHNOLOGY

MBI

E- ISSN : 2985-8321
P -ISSN : 2985-704X

Recent in Engineering Science and Technology (RiESTech)
PT MENCERDASKAN BANGSA INDONESIA (MBI)
Available online at: http://www.mbi-journals.com/index.php/riestech

E- ISSN : 2985-8321
P -ISSN : 2985-704X

Recent in Engineering Science and Technology (RiESTech)

Volume 3 No 4 October 2025

FOCUS AND SCOPE

RIESTECH

Recent in Engineering Science and Technology **(RiESTech):** I*SSN: 2985-704X (print), ISSN: 2985-8321 (online)* a peer-reviewed quarterly engineering journal, publishes theoretical and experimental high-quality papers to promote engineering and technology's theory and practice. In addition to peer-reviewed original research papers, the Editorial Board welcomes original research reports, state-of-the-art reviews, and communications in the broadly defined field of recent engineering science and technology. **RiESTech** covers topics contributing to a better understanding of engineering, material science, computer science, environmental science, and their applications. **RiESTech** is concerned with scientific research on mechanical and civil engineering, Electrical/Electronics and Computer Engineering, and Metallurgical and Materials Engineering with specific analytical techniques and/or computational methods.

The frequency of RiESTech publications is four times a year namely in January, April, July, and October. The scope of RiESTech includes a wide spectrum of subjects namely:

Mechanical and Civil Engineering (Automotive Technologies; Construction Materials; Design and Manufacturing; Dynamics and Control; Energy Generation, Utilization, Conversion, and Storage; Fluid Mechanics and Hydraulics; Heat and Mass Transfer; Micro-Nano Sciences; Renewable and Sustainable Energy Technologies; Robotics and Mechatronics; Solid Mechanics and Structure; Thermal Sciences)

Electrical/Electronics and Computer Engineering (Instrumentation; Coding, Cryptography, and Information Protection; Communications, Networks, Mobile Computing, and Distributed Systems; Compilers and Operating Systems; Parallel Processing, and Dependability; Computer Vision and Robotics; Control Theory; Electromagnetic Waves, Microwave Techniques and Antennas; Embedded Systems; Integrated Circuits, VLSI Design, Testing, and CAD; Microelectromechanical Systems; Microelectronics, and Electronic Devices and Circuits; Power, Energy and Energy Conversion Systems; Signal, Image, and Speech Processing; Machine Learning and Data Science)

E- ISSN : 2985-8321
P -ISSN : 2985-704X

Metallurgical and Materials Engineering (Advanced Materials Science; Ceramic and Inorganic Materials; Electronic-Magnetic Materials; Energy and Environment; Materials Characterization; Metallurgy Extractive; Polymers and Nanocomposites)

Environmental Science and Engineering (Waste Management, Climate Change, Zero Waste, Environmental Disaster Management, Circular Economy, Sustainable Development, Environmental Security, Environmental Management, Environmental Ecology, Conservation of Natural Resources And Environment, Environmental Impact Analysis, Planning and Environmental Administration, Environmental Health, Environmental Pollution, Environmental Accounting, and Environmental Information Systems)

Recent in Engineering Science and Technology (RiESTech)
PT MENCERDASKAN BANGSA INDONESIA (MBI)
Available online at: http://www.mbi-journals.com/index.php/riestech

E- ISSN : 2985-8321
P -ISSN : 2985-704X

Recent in Engineering Science and Technology

(RiESTech)

Volume 3 No 4 October 2025

Recent in Engineering Science and Technology (RiESTech)
PT MENCERDASKAN BANGSA INDONESIA (MBI)
Available online at: http://www.mbi-journals.com/index.php/riestech

E- ISSN : 2985-8321
P -ISSN : 2985-704X

Layout and Typesetting:

Imam Sapto Nugroho, Universitas Indonesia (Alumni), Indonesia
Kamil Raihan Permana, Universitas Indonesia, Indonesia
Raihan Trinanda Agsya, Politeknik Negeri Jakarta, Indonesia

PUBLISHER
PT MENCERDASKAN BANGSA INDONESIA (MBI)
Address : 4th Floor Gedung STC Senayan Room 31-34, Jl. Asia Afrika Pintu IX, Jakarta 10270, Indonesia.

Recent in Engineering Science and Technology (RiESTech)
PT MENCERDASKAN BANGSA INDONESIA (MBI)
Available online at: http://www.mbi-journals.com/index.php/riestech

E- ISSN : 2985-8321
P -ISSN : 2985-704X

Recent in Engineering Science and Technology (RiESTech)

Volume 3 No 4 October 2025

PREFACE

Journal RiESTech (p-ISSN: 2985-704X (print), e-ISSN: 2985-8321 (online); is a peer review journal published by PT Mencerdaskan Bangsa Indonesia. The RiESTech journal is published four times a year in January, April, July, and October. This journal provides direct open access to its content on the principle that making research freely available to the public supports a greater global exchange of knowledge within the engineering field. This journal aims to provide a place for academics, researchers, and practitioners to publish original research articles or review articles. The scope of articles published in this journal relates to various topics in the field of outcomes of research activities.

The RiESTech journal publishes papers strictly following the RiESTech guidelines and templates for manuscript preparation. All submitted manuscripts will go through a double-blind peer review process. The paper is read by members of the editor (according to the area of specialization) and will be screened by the Managing Editor to meet the criteria required for RiESTech publication. Manuscripts will be sent to two reviewers based on their historical experience in reviewing manuscripts or based on their areas of specialization. RiESTech has review forms to keep the same item reviewed by two reviewers. Then the editorial board makes a decision on the comments or suggestions of the reviewers.

Reviewers provide an assessment of originality, clarity of presentation, contribution to the field/science. This journal publishes research articles, review articles/literature reviews, case reports and concept/policy articles, in all fields of Computer Science, Informatics Engineering, Multimedia, Arts. The article to be published is an original work and has never been published. Incoming articles will be reviewed by the reviewer team.

The Editorial Board will try to continue to improve the quality of the journal so that it can become an important reference in the development of engineering sciences. The greatest appreciation and gratitude to Mitra Bestari along with members of the Editorial Board and all parties involved in the publication of this journal. Complete writing instructions are displayed on the portal of this journal.

Regards,

Chief Editor

Recent in Engineering Science and Technology (RiESTech)
PT MENCERDASKAN BANGSA INDONESIA (MBI)
Available online at: http://www.mbi-journals.com/index.php/riestech

E- ISSN : 2985-8321
P -ISSN : 2985-704X

Recent in Engineering Science and Technology (RiESTech)

Volume 3 No 4 October 2025

Contents

Focus and Scope ii
Editor Team iii
Preface v
Contents vi

Articles

- ***Screw Conveyor Design to Reduce Musculoskeletal Disorders (MSDs) Risk in Coconut Shell Handling***
  Fajar Hadi Crisnamurti, Agus Edy Pramono
  1 - 9

- ***Design of a Fertilizer Lifting Crane for the Canycom S25A Fertilizer Spreader Unit***
  Irwan Sukma, Agus Edy Pramono
  10 - 23

- ***Effects of Red Rosela Tea (Hibiscus sabdariffa) as An Organic Inhibitor for Low Carbon Steel in An Environment of Sodium Chloride 3,5%***
  Giafin Bibsy Rahmaulita, Johny Wahyuadi Mudaryoto Soedarsono
  24 - 35

- ***Study of the Effect of Volume of Moringa Leaves and Purple Sweet Potato Extracts as a Green Corrosion Inhibitor on the Corrosion of API 5L Steel Metals in 0.2 M HCl Environments***
  Yudha Pratesa, Kezia, Tio Angger Pertama, Johny Wahyuadi Soedarsono
  36 - 48

- ***Comparing MLP and 1D-CNN Architectures for Accurate RUL Forecasting in Lithium Batteries***
  Idrus Assagaf, Agus Sukandi, Parulian Jannus, Sonki Prasetya, Asep Apriana, Ega Edistria, Abdul Azis Abdillah
  49 - 58

RiESTech
Recent in Engineering Science and Technology

MBI

Article

Screw Conveyor Design to Reduce Musculoskeletal Disorders (MSDs) Risk in Coconut Shell Handling

Fajar Hadi Crisnamurti [1,*], Agus Edy Pramono [1]

[1] Magister Program in Applied Manufacturing Technology Engineering, Politeknik Negeri Jakarta,Jl. Prof. Dr. G.A. Siwabessy, Kampus UI, Depok 16425, Jawa Barat, Indonesia
* Correspondence: fajar.crisnahadi@gmail.com

Abstract: This study aims to analyze the working posture of operators involved in feeding coconut shells into a processing machine, using the Rapid Entire Body Assessment (REBA) method. Data were collected through direct observation and video analysis of workers performing the task over a full work shift, ensuring diverse movement patterns and postures were captured. The assessment yielded a total REBA score of 9, which indicates a high level of ergonomic risk requiring immediate corrective action. This elevated score is attributed to repetitive movements during the material handling process. To mitigate the risk of Musculoskeletal Disorders (MSDs), a specially designed portable screw conveyor is proposed as an assistive tool. The proposed conveyor is expected to significantly reduce physical strain and improve the overall ergonomics of the task by minimizing repetitive lifting and awkward postures. Visual illustrations of the design and technical drawing are provided to support the implementation concept. This study highlights the importance of ergonomic interventions in industrial settings to promote worker health and operational efficiency.

Keywords: Material Handling; Ergonomic worker; Rapid Entire Body Assesment (REBA); Coconut Shell

Citation:. Crisnamurti, F. H., Pramono, A. E. (2025). Screw Conveyor Design to Reduce Musculoskeletal Disorders (MSDs) Risk in Coconut Shell Handling. Recent in Engineering Science and Technology, 3(04), 1–9. Retrieved from https://www.mbi-journals.com/index.php/riestech/article/view/99

Academic Editor: Vika Rizkia

Received: 8 April 2025
Accepted: 10 June 2025
Published: 31 October 2025

Publisher's Note: MBI stays neutral with regard to jurisdictional claims in published maps and institutional affiliations.

1. Introduction

The manual process of feeding chopped coconut shells into a shredding machine often leads to physical fatigue among workers. This task requires continuous lifting and inserting of coconut shells over extended periods, resulting in muscle strain and increasing the risk of work-related injuries. Repetitive movements and awkward postures contribute significantly to ergonomic hazards like Musculoskeletal Disorders (MSDs), which are among the most common occupational injuries in labor-intensive environments[1]. The entire handling process including transferring coconut shells from storage, placing them into backets, transporting them to the shredder machine, and subsequently tidying up the area is carried out manually. Due to production targets, little attention is paid to workers' posture during these repetitive tasks, further elevating ergonomic risks[2].

Despite the widespread use of coconut shells in biomass energy and other industrial applications, the broader significance of improving this processing step, particularly in terms of worker safety and productivity, remains underreported. According to a study by the International Labor Organization (ILO), ergonomic risk account for over 30% of all workplace-related injuries in manual material handling operations[3]. However, localized data and case studies

on the ergonomic impacts of coconut shell processing in Indonesia or similar contexts remain limited.

To address these issues, this study proposes the design and development of a portable conveyor system as an ergonomic intervention aimed at reducing physical workload. The conveyor system is designed for mobility and flexibility, allowing the equipment to be relocated as needed depending on the workflow layout. The proposed conveyor is constructed using mild steel for the frame, a wear-resistant rubber belt for material transport, and castor wheels to enhance portability. The drive system employs a low-power electric motor to ensure energy efficiency and operational sustainability.[4]

The manufacturing process involves cutting, welding, and modular assembly of components, which simplifies maintenance and enhances the system's adaptability in various work settings. This proposed design is expected to improve productivity, minimize injury risks, and provide flexible application across multiple workplace environments. The following figures illustrate the three-dimensional design concept, the coconut shell handling process, and the associated worker postures[5].

2. Materials and Experiment Methods

The design process began with problem identification through direct observation at the PT GKI Cibinong Bogor Plant, specifically in the coconut shell processing area at the Production Department section. A field study was conducted using interviews and on-site observations. A detailed case analysis was carried out using the Rapid Entire Body Assessment (REBA) method. Supporting tools used in this research included a weighing scale, ruler, and measuring tape. In addition, AutoCAD software was utilized to evaluate the operator's working posture[6].

The REBA method is an ergonomic assessment tool designed to evaluate the overall posture of the human body, covering the neck, back, arms, wrists, and legs [7]. This method is particularly relevant for addressing common ergonomic issues faced by workers in small and medium-sized enterprises. The REBA score is influenced by external forces acting on the object being handled and the nature of the work activity itself [8]. This method enables a relatively quick evaluation and provides a general overview of the activities that require immediate intervention to reduce the risk associated with operator work behavior.[9]

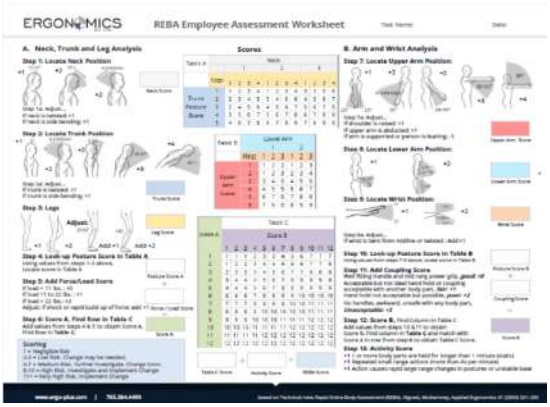

Figure 1. Worksheet REBA [10]

Data collection involved documenting one of the operators while performing the task. The results were then analyzed and compiled into a table format based on the REBA Employee Assessment Worksheet, as shown in Appendix Figure 1. The first step in the Rapid Entire Body Assessment (REBA) method involves the evaluation of working posture, which is categorized into two groups. Group A includes the trunk, legs, and neck, while Group B consists of the upper arm (shoulder), lower arm (elbow), and wrist [11]. During the process of lifting coconut shells into the machine, each of these body components is assessed and assigned a score based on the observed working posture[12].

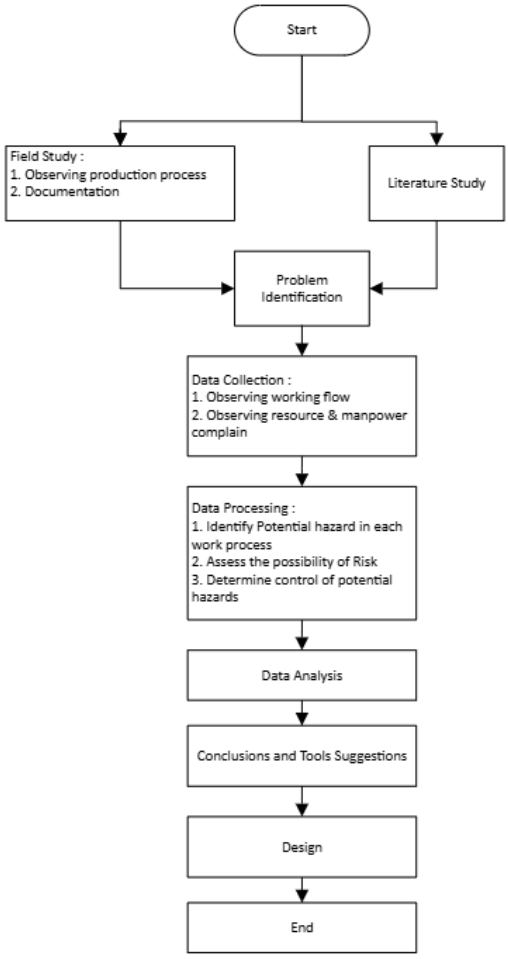

Figure 2. Flow Diagram

The workflow diagram in Figure 2. Illustrates the systematic approach used in this study to identify hazards and propose appropriate design interventions in the coconut shell feeding process. The process begins with a field study consisting of direct observation of production activities and documentation of worker routines, this also supported by a Literature Study. These two initial inputs lead to Problem Identification, where specific issues related to manual handling and worker posture are defined[13].

Following problem identification, Data Collection is conducted, focusing on two key activities: observing the workflow and documenting feedback or complaints from the workforce.[14] These observations serve as the foundation for Data Processing, which involvherehree critical steps: identifying potential hazards in each task, assessing the associated

risks, and determining possible control measures to minimize those hazards. The evaluation results are then referenced against the REBA action level chart [15], as presented in Table 1.

Table 1. REBA Action Level.

Total Score	Risk Level	Corrective Action
1	Neglected	Not Necessary
2-3	Low	Might Be Necessary
4-7	Medium	Needed
8-10	High	Needed As Soon As Possibly
11-15	Very High	Required Now

Subsequently, the study proceeds to Data Analysis, where the collected information is evaluated to understand the relationship between manual handling activities and ergonomic risk. Based on the analysis, the next stage involves drawing Conclusions and Suggesting Tools, including potential ergonomic interventions such as the use of a portable conveyor system. The final stage is the Design phase, where proposed solutions are translated into technical specifications, followed by implementation planning[16].

This structured methodology ensures that the solution is grounded in empirical observations and aligned with ergonomic safety standards, ultimately aiming to improve worker well-being and operational efficiency.

3. Results and Discussion

The posture assessment process begins with capturing photographs using a camera. The resulting images are utilized to determine the angular measurements of each body segment. The body parts evaluated include the neck, back, legs, upper arms, lower arms, and wrists. These angles are analyzed to assess the posture of the worker during the activity. The angle assessment of the worker's posture is illustrated in Figure 3 below.

3.1. Assesment of Worker Body Posture Angles

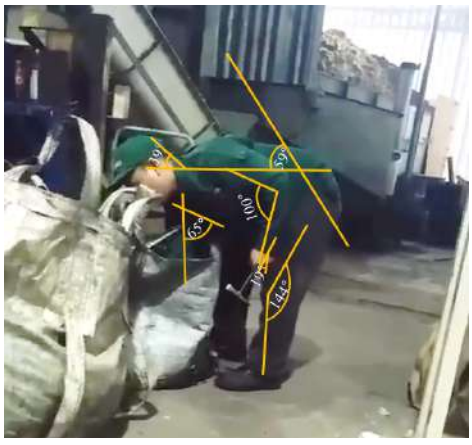

Figure 3 Worker Body Posture Angles

Figure 3 Illustrates the ergonomic assessment of a worker's body posture during the coconut shell feeding process using the the REBA (Rapid Entire Body Assesment) method. The

image captures a real-time scenario where the worker is manually transferring chopped coconut shells from a storage bag into a container. The body angles measured included the neck (39° flexion), trunk (59° bending), upper arm (65° elevation), fore arm (100°), and feet (144° flexion), all of which indicate awkward and strained postures.

This static posture involves significant bending of the back and knees while simultaneously elevating the arms, contributing to a high ergonomic risk score. Such posture, if repeated frequently without proper intervention, can lead to musculoskeletal disorders, particularly in the lower back, shoulders, and feet or knees. The REBA analysis based on these angles suggests that the task falls within a high-risk category, requiring immediate ergonomic improvement or redesign of the work method.

Table 2. Worker Body Postures Angles

Number	Body Part					
	Neck	Back	Feet	Upper Arm	Fore arm	Wrist
Fig.3	A 39°	A 59°	A 144°	A 65°	A 100°	A 19°
Score	3	3	2	3	2	2

3.1.1. Score A

Table A		Neck											
		1				2				3			
	Legs	1	2	3	4	1	2	3	4	1	2	3	4
Trunk Posture Score	1	1	2	3	4	1	2	3	4	3	3	5	6
	2	2	3	4	5	3	4	5	6	4	5	6	7
	3	2	4	5	6	4	5	6	7	5	6	7	8
	4	3	5	6	7	5	6	7	8	6	7	8	9
	5	4	6	7	8	6	7	8	9	7	8	9	9

Figure 4 Score A in REBA Worksheet

Figure 4 presents the calculation of Score A in the REBA worksheet, which focuses on the postures of the neck, trunk, and legs during the task. Based on the postures angles observed in the previous figure (Figure 3), the scoring results are as follows: a score of 3 for the trunk posture due to a significant forward bend, 3 for the neck due to moderate flexion, and 2 for the leg position based on the semi-squat stance.

These scores are cross-referenced in the REBA Table A matrix, resulting in a combined posture score of 6. Since the load handled by the worker is under 4.9kg (11lbs), no additional load or force score is added at this stage. This Score A indicates a moderate risk level and serves as an early warning that ergonomic improvements-such as workstation redesign or mechanical aids should be considered to prevent long-term musculoskeletal disorders.

3.1.2. Score B

Table B		Lower Arm					
		1			2		
	Wrist	1	2	3	1	2	3
Upper Arm Score	1	1	2	2	1	2	3
	2	1	2	3	2	3	4
	3	3	4	5	4	5	5
	4	4	5	5	5	6	7
	5	6	7	8	7	8	8
	6	7	8	8	8	9	9

Figure 5 Score B in REBA Worksheet

Figure 5 illustrates the calculation of Score B in the REBA Worksheet, which evaluates the posture of the upper limb segments namely the upper arm, lower arm, and wrist. In this assessment, the upper arm scores a 3 due to shoulder elevation and forward reach, the lower arm receives a 2 based on its angle, and the wrist also scores 2 due to a slight bend and deviation from neutral postures.

When these values are referenced in Table B, the combination results in a posture score of 5. This score reflects a moderate level of ergonomic risk for the upper extremities during the task. As the object being handled is not considered heavy, no additional force or coupling points are added. This indicates a need for improvement in arm posture possibly by redesigning the workstation layout or using supportive equipment to reduce strain on the shoulders and wrists during prolonged tasks.

3.1.3. Total Score A + B

Score A	Table C Score B											
	1	2	3	4	5	6	7	8	9	10	11	12
1	1	1	1	2	3	3	4	5	6	7	7	7
2	1	2	2	3	4	4	5	6	6	7	7	8
3	2	3	3	3	4	5	6	7	7	8	8	8
4	3	4	4	4	5	6	7	8	8	9	9	9
5	4	4	4	5	6	7	8	8	9	9	9	9
6	6	6	6	7	8	8	9	9	10	10	10	10
7	7	7	7	8	9	9	9	10	10	11	11	11
8	8	8	8	9	10	10	10	10	10	11	11	11
9	9	9	9	10	10	10	11	11	11	12	12	12
10	10	10	10	11	11	11	11	12	12	12	12	12
11	11	11	11	11	12	12	12	12	12	12	12	12
12	12	12	12	12	12	12	12	12	12	12	12	12

Figure 6 Total Score

Figure 6 displays the final calculation based on the Rapid Entire Body Assessment (REBA) worksheet score by combining Score A and Score B using Table C. In this assessment, Score A is 6, derived from trunk, neck, and leg posture analysis, while Score B is 5, based on the upper limb positioning (as detailed in Figure 5). When these two values intersect in Table C, the result is a combined score of 8.

However, considering that the task being evaluated is performed repetitively, an additional point is added, resulting in a final Group C score of 9. This score falls into the category of high

risk, signaling that immediate ergonomic intervention is required to prevent musculoskeletal disorders and improve workplace safety.

The high REBA score justifies the need for design modifications or assistive tools. In this context, the article proposes the implementation of a portable conveyor system to handle coconut shell materials more efficiently and ergonomically. This solution is intended to reduce strain on the worker's posture and improve productivity, as illustrated in Figres 7 and 8.

Figure 7 Design Conveyor Portable

Figure 7 shows the 3D Design of the proposed portable conveyor that serves as an ergonomic intervention tool in the coconut shell handling process. This conveyor is specifically designed to reduce manual lifting and bending activities, which contribute significantly to musculoskeletal risk as identified in the REBA assessment. The structure is constructed from lightweight yet durable materials to ensure portability and ease of relocation in a workshop or factory setting. The slanted configuration enables the material to move upward efficiently, thereby minimizing physical strain on workers during material transfer.

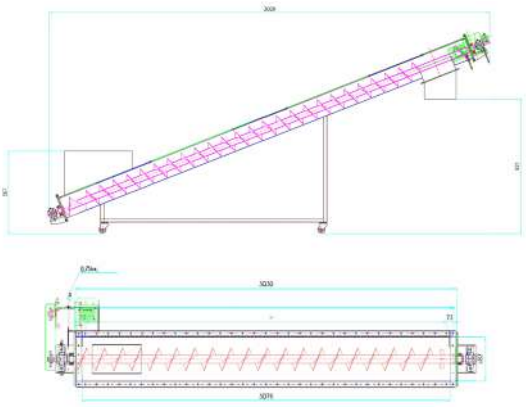

Figure 8 Drawing Conveyor Portable

Figure 8 presents the technical draing of the conveyor design, showcasing its dimensional specifications and mechanical configuration. The conveyor has a total length of 3076mm with a transport inclination angle that optimizes material movement while maintaining stability. The side view illustrates the internal screw mechanism that aids in transporting the coconut shells, while the top view reveals the spatial layout of the motor, screw shaft, and casing. These detailed engineering visuals serve as a blueprint for fabrication and emphasize the importance

of ergonomic design in equipment manufacturing, ensuring both worker safety and operation efficiency.

4. Conclusions

Several conclusions can be drawn from the study on operator posture analysis, which reveals a high potential for triggering symptoms of Musculoskeletal Disorders (MSDs). Using the Rapid Entire Body Assessment (REBA) method, the assessment of worker posture during the process of inserting coconut shells into the machine resulted in a REBA score of 9. This score indicates that immediate corrective action is necessary to reduce the risk of worker injury.

To address this ergonomic issue, the implementation of an assistive tool specifically a Portable Screw Conveyor is proposed. This tool significantly mitigates the risk of MSDs by eliminating repetitive lifting, bending, and twisting motions, which are common when feeding coconut shells manually. The conveyor system allows for continuous, controlled material flow, thereby maintaining a neutral posture for operators, minimizing spinal stress, and reducting static load on the upper limbs and back. Such mechanical intervention reduces physical strain and improves overall occupational health during the coconut shell feeding process.

Acknowledgments: the author would like to thank everyone who has contributed ideas and terials. Second, the author would like to express gratitude to PT GKI for providing the equipment used in this study. Third, in recognition of their time and efforts in supporting this research, the author thanks to the person in material handling employees.

References

1. B. Md. Deros, D. D. I. Daruis, A. R. Ismail, and A. R. A. Rahim, "Work posture and back pain evaluation in a Malaysian food manufacturing company," *American Journal of Applied Sciences*, vol. 7, no. 4, pp. 473–479, 2010, doi: 10.3844/ajassp.2010.473.479.
2. M. Rajendran, A. Sajeev, R. Shanmugavel, and T. Rajpradeesh, "Ergonomic evaluation of workers during manual material handling," *Mater Today Proc*, vol. 46, pp. 7770–7776, 2021, doi: 10.1016/j.matpr.2021.02.283.
3. L. M. Wings, H. Foot, P. Taschner, V. Kretschmer, and M. Riester, "Distribution of physical workload with an ergonomic order assignment," in *IFAC-PapersOnLine*, Elsevier B.V., Aug. 2024, pp. 205–210. doi: 10.1016/j.ifacol.2024.09.161.
4. R. G. Thomas, C. E. van Baar, and M. J. van der Stee, "Baggage handling postures and the design of conveyors," *Applied Ergonomics*, vol. 26, no. 2, pp. 123–127, Apr. 1995, doi: 10.1016/0003-6870(95)00005-W.
5. T. Engström, J. J. Hanse, and R. Kadefors, "Musculoskeletal symptoms due to technical preconditions in long cycle time work in an automobile assembly plant: A study of prevalence and relation to psychosocial factors and physical exposure," *Applied Ergonomics*, vol. 30, no. 5, pp. 443–453, 1999, doi: 10.1016/S0003-6870(98)00059-3.
6. K. N. S. B. K. Ismail, S. N. Basah, N. H. B. Omar, M. Murugappan, and S. B. Yaacob, "Mathematical modeling of human body for lifting task," *Proceedings - 2012 IEEE International Conference on Control System, Computing and Engineering, ICCSCE 2012*, no. July 2014, pp. 149–154, 2012, doi: 10.1109/ICCSCE.2012.6487132.

7. M. Middlesworth, "A Step-by-Step Guide Rapid Entire Body Assessment (REBA)," *Ergonomics Plus Inc*, vol. 31, pp. 1–11, 2021.
8. T. M. Akbar, A. Erik Nugraha, and W. Eko Cahyanto, "Analisis Postur Tubuh Pekerja di Pabrik Roti Riza Bakery Menggunakan Metode Rapid Entire Body Assessment (REBA)," *Journal of Integrated System*, vol. 6, no. 1, pp. 32–41, 2023, doi: 10.28932/jis.v6i1.6004.
9. T. Baskaran, K. Sankaranarayanasamy, and K. Gopanna, "Musculoskeletal disorder risk levels in mobile crane operators: An ergonomic assessment," *Mater Today Proc*, vol. 72, pp. 3089–3092, Jan. 2023, doi: 10.1016/j.matpr.2022.09.252.
10. V. Bhatia, P. Kalra, and J. S. Randhawa, "Ergonomic Interventions for Manual Material Handling Tasks in a Warehouse," no. December, pp. 205–212, 2021, doi: 10.1007/978-981-15-9054-2_23.
11. N. R. Kodle, S. P. Bhosle, and V. B. Pansare, "Ergonomic risk assessment of tasks performed by workers in granite and marble units using ergonomics tool's REBA," *Mater Today Proc*, vol. 72, pp. 1903–1916, Jan. 2023, doi: 10.1016/J.MATPR.2022.10.153.
12. K. Enez and S. S. Nalbantoğlu, "Comparison of ergonomic risk assessment outputs from OWAS and REBA in forestry timber harvesting," *Int J Ind Ergon*, vol. 70, pp. 51–57, Mar. 2019, doi: 10.1016/j.ergon.2019.01.009.
13. S. Zargarzadeh, M. Bahramian, M. Mohseni, and N. Arjmand, *Comparison of ten widely-use ergonomic risk assessment tools based on evaluations of various manual materials handling activities*, vol. 0, no. 0. 2024. doi: 10.24200/sci.2024.63530.8451.
14. L. K. Sharma, M. K. Sain, M. L. Meena, and G. S. Dangayach, "An Investigation of Ergonomic Risk for Work-Related Musculoskeletal Disorders with Hand-Held Drilling," *Evergreen*, vol. 10, no. 1, pp. 36–42, 2023, doi: 10.5109/6781034.

RiESTech
Recent in Engineering Science and Technology

MBI

Article

Design of a Fertilizer Lifting Crane for the Canycom S25A Fertilizer Spreader Unit

Irwan Sukma [1,*], Agus Edy Pramono [1]

[1] Magister Program in Applied Manufacturing Technology Engineering, Politeknik Negeri Jakarta,Jl. Prof. Dr. G.A. Siwabessy, Kampus UI, Depok 16425, Jawa Barat, Indonesia
* Correspondence: irwan.sukma.tm24@stu.pnj.ac.id

Abstract: Manual lifting of fertilizer bags in plantation operations often leads to musculoskeletal disorders (MSDs) among workers due to repetitive, high-load, and ergonomically poor movements. This study aims to design an ergonomic fertilizer lifting crane integrated into the Canycom S25A Fertilizer Spreader with a 650-liter hopper to reduce physical strain and improve operational efficiency. A hydraulic crane system was designed with dual-segment arms, four lifting hooks, and two hydraulic cylinders, actuated via the unit's PTO engine. Ergonomic evaluation was performed using the REBA assessment tools. The simulation results indicated that the maximum stress on critical components was within safe limits, with a factor of safety above 1.5. Postural analysis showed a significant improvement, where REBA scores decreased from 12 to 2 after the crane was introduced. The design offers a reliable, low-cost, and easily manufactured solution that enhances worker safety, reduces ergonomic risk, and increases productivity in fertilizer loading processes, especially in rugged field environments. The crane can be adopted in various agricultural applications where safe material handling is essential.

Keywords: Ergonomics; Fertilizer Lifting Crane; Hydraulic; REBA; Agricultural Mechanization

Citation:. Sukma, I., Pramono, A. E. (2025). Design of a Fertilizer Lifting Crane for the Canycom S25A Fertilizer Spreader Unit. Recent in Engineering Science and Technology, 3(04), 10–23. Retrieved from https://www.mbi-journals.com/index.php/riestech/article/view/101

Academic Editor: Noor Hidayati

Received: 7 April 2025
Accepted: 31 May 2025
Published: 31 October 2025

Publisher's Note: MBI stays neutral with regard to jurisdictional claims in published maps and institutional affiliations.

1. Introduction

Fertilizer application in large-scale agricultural and plantation operations remains a labor-intensive task, especially during the loading phase into hopper spreaders such as the Canycom S25A. Despite advancements in mechanization, many field operators are still required to manually lift and pour fertilizer bags weighing up to 50 kg into elevated hoppers. This repetitive and physically demanding process increases the risk of musculoskeletal disorders (MSDs), fatigue, and long-term injury[1]. Furthermore, uneven terrain and extended working hours exacerbate these ergonomic challenges [2].

Numerous studies have shown that poor manual handling practices in agriculture contribute significantly to lost working time and decreased productivity [3][4]. Although some mechanized aids such as hydraulic arms and robotic lifters have been introduced in industrial sectors [5][6], their application in the agricultural domain—particularly in compact, mobile field units—remains limited. Existing solutions often lack adaptability, are costly, or are not ergonomically optimized for the variability of field conditions [7] [8].

To address this gap, recent research has focused on integrating ergonomic design with functional agricultural machinery. One promising approach is the use of hydraulic crane systems powered by onboard PTO (Power Take-Off) engines, which allow seamless integration with

existing mobile spreader units [9]. Studies incorporating ergonomic assessments using tools like REBA and RULA have demonstrated substantial reductions in operator strain when mechanical lifting aids are used [10], [11][12].

This study aims to design an ergonomic fertilizer lifting crane that mechanical lifting system specifically designed to handle fertilizer bags while minimizing physical strain, injury risk, and discomfort for the operator, specifically tailored to the Canycom S25A Fertilizer Spreader, equipped with a 650-liter hopper. The system is designed to lift four 50-kg fertilizer bags simultaneously using a foldable hydraulic boom arm and four-point hook mechanism. The work simulation with ergonomic assessment to ensure safety, reliability, and usability in real field conditions.

Figure 1. Manual Lifting Fertilizer

The key contribution of this study is the development of a compact, integrated lifting solution that improves operator safety while maintaining functional and mechanical compatibility with existing agricultural machinery. The findings provide a blueprint for enhancing mechanization in small and medium-scale farming, reducing the reliance on manual labor in high-risk activities.

2. Materials and Experiment Methods

The design of the fertilizer lifting crane was developed using a structured engineering design approach combining ergonomic analysis, CAD modeling, structural simulation, and prototype manufacturability. The core design is integrated with the Canycom S25A Fertilizer Spreader, using its PTO (Power Take-Off) engine as the hydraulic power source.

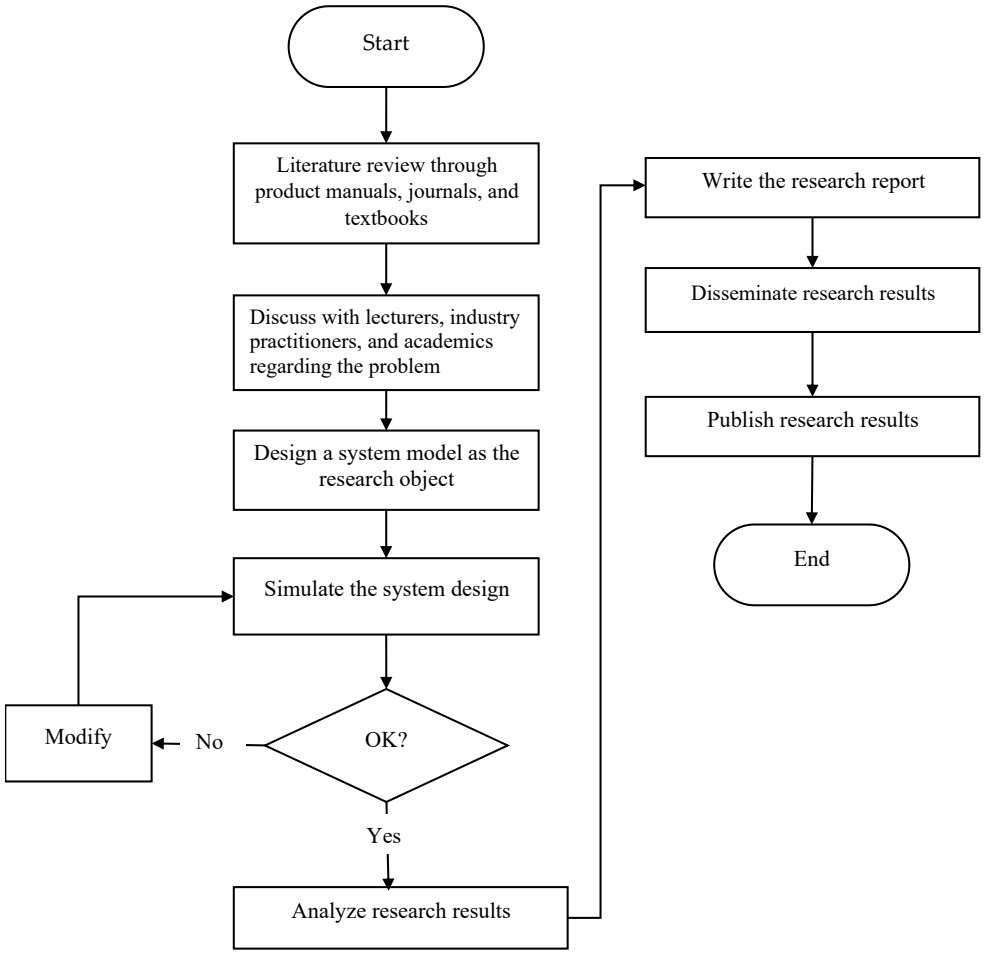

Figure 2. Research Flow Process

The crane structure was fabricated using SS400 carbon steel hollow square pipe (50 mm × 50 mm × 5 mm), chosen for its strength, weldability, and cost-efficiency. SS400 is a widely used structural carbon steel grade under Japanese Industrial Standards (JIS G3101), known for its excellent balance of strength, ductility, weldability, and cost. It is a mild steel with a typical yield strength of 245 MPa and tensile strength ranging between 400–510 MPa, making it suitable for general-purpose structures including cranes, frames, and agricultural machinery.

The crane structure utilizes 50 mm × 50 mm × 5 mm hollow square pipe fabricated from SS400. This profile provides a high moment of inertia, allowing it to resist bending and shear forces under working loads. In this application, the crane is designed to lift up to 250 kg (equivalent to 4 fertilizer bags at 50 kg each + margin). Based on Finite Element Method (FEM) simulations, the maximum stress induced under full load is 159 MPa, well below the material's yield strength, with a safety factor greater than 1.5, indicating a structurally sound design. From a fabrication perspective, SS400 offers excellent weldability without requiring preheating, which simplifies manufacturing and ensures strong, reliable joints. Its ductility and machinability also facilitate processes such as cutting, drilling, and fitting hydraulic components. In terms of cost, SS400 is more economical than higher-grade alloy steels or stainless steels, making it a cost-effective solution for heavy-duty yet budget-sensitive applications like agricultural crane

systems. Its global availability further supports ease of sourcing and scalability for field fabrication or mass production.

Hydraulic components include two double-acting cylinders with a bore diameter of 25 mm and a stroke length of 300 mm. Four steel hooks are installed at the arm end to carry four 50-kg fertilizer bags simultaneously. Joints and pivots use standard steel pins and greaseable bushings. Control is provided through a manual hydraulic lever mounted beside the operator's seat. The entire structure was modeled in SolidWorks 2022, including the boom arm, mounting brackets, hydraulic actuators, and hopper interface. The arm is divided into two foldable segments (vertical and horizontal), each measuring 800 mm, allowing compact storage when not in use.

REBA (Rapid Entire Body Assessment) is a systematic method for evaluating working posture to assess the overall risk level on the body based on posture angles, load handling, repetitive movements, and hand coupling. This method does not require expensive equipment and can be applied in the field using only a scoring worksheet and direct observation.

The REBA evaluation divides the body into two groups:

- Group A: neck, trunk, and legs
- Group B: upper arm, lower arm, and wrist

The final score is obtained by combining posture assessment, applied force, activity frequency, and grip quality. The ergonomic impact was assessed using REBA (Rapid Entire Body Assessment) methods. Pre- and post-design posture scores were recorded using direct observation, video capture, and analysis via worksheets following ISO 11228-1 guidelines. Scores were used to evaluate improvement in musculoskeletal disorder risk.

Tabel A		Neck											
		1				2				3			
	Legs	1	2	3	4	1	2	3	4	1	2	3	4
Trunk Posture Score	1	1	2	3	4	1	2	3	4	3	3	5	6
	2	2	3	4	5	3	4	5	6	4	5	6	7
	3	2	4	5	6	4	5	6	7	5	6	7	8
	4	3	5	6	7	5	6	7	8	6	7	8	9
	5	4	6	7	8	6	7	8	9	7	8	9	9

Figure 3. Group A Score REBA Worksheet Manual Lifting

When lifting a 50 kg fertilizer bag manually, the operator bends the neck (20°), trunk (20–60°), and knees deeply, resulting in REBA scores of 1 (neck), 2 (trunk), and 4 (legs). These values produce a Posture Score A of 5, indicating a moderate risk. This posture puts stress on the lower back and knees, especially when repeated. The assessment supports the need for ergonomic lifting aids to reduce musculoskeletal strain and improve safety.

Tabel B		Lower Arm					
		1			2		
	Wrist	1	2	3	1	2	3
Upper Arm Score	1	1	2	2	1	2	3
	2	1	2	3	2	3	4
	3	3	4	5	4	5	5
	4	4	5	5	5	6	7
	5	6	7	8	7	8	8
	6	7	8	8	8	9	9

Figure 4. Group B Score REBA Worksheet Manual Lifting

During the manual lifting of a 50 kg fertilizer bag, the operator extends the upper arm beyond 90°, resulting in an Upper Arm Score of 6. The lower arm is positioned between 60–100°, which corresponds to a Lower Arm Score of 2. Additionally, the wrist is angled beyond 15°, resulting in a Wrist Position Score of 3.

Using REBA Table B to assess the combined posture of the upper extremities, these values yield a Posture Score B of 9, indicating a high ergonomic risk. This posture places excessive strain on the shoulders, elbows, and wrists, particularly when handling heavy loads like fertilizer bags. Repeated exposure to this position can lead to overuse injuries and long-term musculoskeletal disorders

Score A (score from table A +load/force score)	Tabel C											
	Score B, (table B value +coupling score)											
	1	2	3	4	5	6	7	8	9	10	11	12
1	1	1	1	2	3	3	4	5	6	7	7	7
2	1	2	2	3	4	4	5	6	6	7	7	8
3	2	3	3	4	5	5	6	7	7	8	8	8
4	3	4	4	5	6	6	7	8	8	9	9	9
5	4	4	4	5	6	6	8	9	9	9	9	9
6	6	6	6	7	8	8	9	9	10	10	10	10
7	7	7	7	8	9	9	10	10	11	11	11	11
8	8	8	8	9	9	10	10	10	11	11	11	11
9	9	9	9	10	10	10	11	11	12	12	12	12
10	10	10	10	10	11	11	11	12	12	12	12	12
11	11	11	11	11	12	12	12	12	12	12	12	12
12	12	12	12	12	12	12	12	12	12	12	12	12

Figure 5. Group C Final Score REBA Worksheet Manual Lifting

In the manual lifting of a 50 kg fertilizer bag, the initial Posture Score A derived from neck, trunk, and leg posture was 5. According to REBA Step 5, an additional +2 points are added due to the high load (≥20 kg), resulting in a final Score A of 7. For the upper limb posture, the

calculated Posture Score B was 9, and an additional +2 points were added for poor coupling (no proper handle or grip), giving a Score B of 11.

Using Table C with Score A = 7 and Score B = 11, the REBA Score C = 11.

Finally, since the task requires holding multiple body parts in a strained position for more than 1 minute (static loading), an Activity Score of +1 is added, yielding a Final REBA Score of 12. This score indicates a very high risk, requiring immediate ergonomic intervention, such as the implementation of mechanical lifting aids to reduce the risk of musculoskeletal disorders (MSDs).

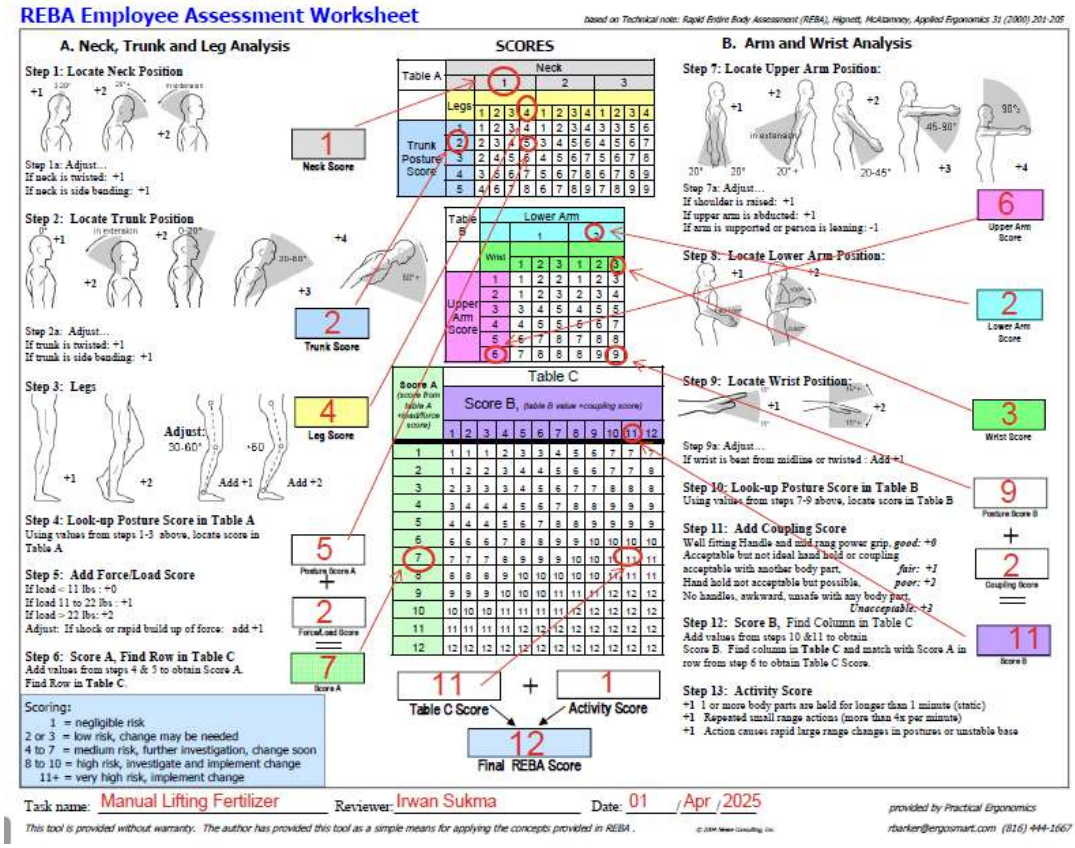

Figure 6. Complete REBA Worksheet Assessment Manual Lifting

Table 1: Level Mosculardisorder REBA

Total Score	Risk Level	Corrective Action
1	Neglected	Not necessary
2–3	Low	Might be necessary
4–7	Medium	Needed
8–10	High	Needed as soon as possible
11–15	Very High	Required now

3. Results and Discussion

3.1 Selected Design Choice

After evaluating three design alternatives, a foldable two-segment hydraulic crane was selected as the optimal solution due to its ergonomic performance, operational efficiency, safety, and integration compatibility with the Canycom S25A Fertilizer Spreader. This crane is designed to lift four fertilizer bags (each 50 kg) simultaneously, using a simple manual hydraulic lever control system.

The crane operates using power from the Kubota V2203 PTO engine onboard the Canycom unit, eliminating the need for external power. Two hydraulic cylinders (vertical and horizontal) provide two degrees of movement, enabling the crane arm to lift and swing the bags precisely above the hopper inlet.

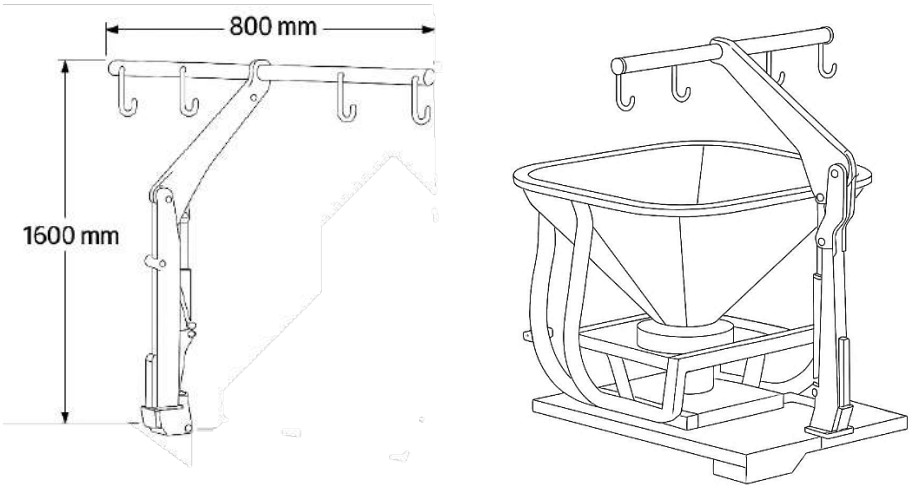

Figure 7. Design Fertilizer Crane

Design Specifications:

- Numbered lists can be noted as follows:
- Lifting Capacity: 250 kg (4 x 50 kg + safety margin)
- Arm Dimensions: 800 mm vertical + 800 mm horizontal
- Number of Hooks: 4
- Hydraulic Cylinders: Ø25 mm bore, 300 mm stroke
- Material: SS400 carbon steel hollow section (50×50×5 mm)
- Control System: Manual hydraulic lever
- Storage Mode: Foldable arm with locking mechanism

Figure 8. Unit Canycom S25A with Crane Fertilizer

3.2 Working Mechanism

The operator rotates the seat rearward to face the crane. Activating the vertical cylinder lifts the first arm segment, followed by the horizontal cylinder moving the second arm to position the load over the hopper. The four hooks collectively lift and release the fertilizer bags. After loading, the arm is returned and locked in its resting position.

3.3 Power and Stress Analysis

a. Power Analysis

The required power is supplied by the PTO engine (Kubota V2203, 45 hp ≈ 33,100 W). The hydraulic pump produces a pressure of 10 MPa with a flow rate of 25 L/min. With a cylinder diameter of 25 mm:

The required hydraulic power P is calculated using the following formula:

$$P = \frac{F \cdot v}{\eta}$$

To lift 250 kg over a distance of 0.8 m in 10 seconds:

$$v = \frac{0.8}{10} = 0{,}08\ \frac{m}{s}$$

$$F = m\,.\,g = 250\ kg\ x\ 9.81\ \frac{m}{s^2} = 2452{,}5\ N$$

$$P = \frac{2452.5\ x\ 0.08}{0.85} \approx 230{,}8\ W$$

This power requirement is supplied by the PTO engine of the Canycom S25A unit (46 HP ≈ 33.1 kW), which is more than sufficient for the system.

b. Maximum Lifting Force:

The maximum lifting force is calculated as:

$$F = m \,.\, g = 250\ kg\ x\ 9.81\ \frac{m}{s^2} = 2.452{,}5\ N$$

c. Force and Moment Analysis on the Crane Arm

The crane consists of two arm segments:

- Vertical segment (base arm): 800 mm
- Horizontal segment (boom arm): 800 mm
- Total arm length: 1600 mm

The force acts at the boom tip, generating a bending moment:

$$M = F\ \cdot L = 2.452{,}5\ N\ x\ 0{,}8\ m = 1.962\ Nm$$

d. Bending Stress on the Arm

$$\sigma = \frac{M\ \cdot y}{I}$$

Where:

M = Bending moment = 1962 Nm
y = Distance from neutral axis to outer fiber (for 50×50×5 mm hollow section, y ≈ 25 mm)
I = Moment of inertia (for hollow square section)

$$I = \frac{(b_{outer}^4\ -\ b_{inner}^4)}{12}$$

$$I = \frac{(0{,}05^4 - 0{,}04^4)}{12} = 2{,}37\ x\ 10^{-8}\ m^4$$

calculated as:

$$\sigma = \frac{1.962\ \cdot 0{,}025}{2{,}37\ x\ 10^{-8}} = 2{,}07\ x\ 10^7 = 20{,}7\ Mpa$$

The resulting stress remains below the elastic limit of SS400 steel (σ_{yield} ≈ 245 MPa), confirming the design's safety.

e. Shear Stress on Pins/Hinges

At the joint between segments and the hydraulic actuator (assumed double shear):

To keep shear stress below the allowable limit (≤ 100 MPa), the minimum pin diameter is calculated:

$$100\ x\ 10^6 = \frac{4.905}{\pi\ d^2} \rightarrow d \approx 8\ mm$$

In practice, Ø10–12 mm pins are used to ensure safety.

f. Safety Factor

$$SF = \frac{\sigma_{yield}}{\sigma_{maks}} \approx 11.83$$

The calculated safety factor confirms that the design is very safe. A recommended range of SF between 2–4 indicates a strong yet potentially optimizable structure in terms of weight and cost.

3.4 Ergonomic Evaluation

The design of the fertilizer lifting crane for the Canycom S25A unit specifically incorporates ergonomic considerations to address common issues associated with manual handling of fertilizer bags. Based on ergonomic work assessments, lifting heavy loads such as 50-kg fertilizer bags without assistive devices imposes excessive strain on the lower back, shoulders, and knees. This not only reduces operational efficiency but also increases the long-term risk of musculoskeletal disorders (MSDs).

To address these concerns, an ergonomic intervention was introduced by replacing manual lifting with a mechanical hydraulic system. The operator no longer directly lifts heavy loads but instead operates a hydraulic lever positioned ergonomically to the right of the seated position. The operator's seat can be rotated to face the crane without needing to dismount from the unit, allowing the task to be performed in a safe, neutral posture.

Tabel A		Neck											
		1				2				3			
	Legs	1	2	3	4	1	2	3	4	1	2	3	4
Trunk Posture Score	1	1	2	3	4	1	2	3	4	3	3	5	6
	2	2	3	4	5	3	4	5	6	4	5	6	7
	3	2	4	5	6	4	5	6	7	5	6	7	8
	4	3	5	6	7	5	6	7	8	6	7	8	9
	5	4	6	7	8	6	7	8	9	7	8	9	9

Figure 9. Group A Score REBA Worksheet Hydraulic Crane Fertilizer

Using REBA Table A with the combination of Neck Score: 1, Trunk Score: 1, and Leg Score: 1, the resulting Posture Score A is 1. This indicates a negligible risk level, meaning no ergonomic intervention is required. The improvement in posture compared to manual lifting scenarios demonstrates the effectiveness of integrating a hydraulic crane in reducing physical strain and optimizing operator safety in fertilizer handling tasks.

Tabel B		Lower Arm					
		1			2		
	Wrist	1	2	3	1	2	3
Upper Arm Score	1	1	2	2	1	2	3
	2	1	2	3	2	3	4
	3	3	4	5	4	5	5
	4	4	5	5	5	6	7
	5	6	7	8	7	8	8
	6	7	8	8	8	9	9

Figure 10. Group B Score REBA Worksheet Hydraulic Crane Fertilizer

In the operation of the hydraulic crane for fertilizer lifting, the upper limb posture was evaluated using REBA Table B. The upper arm was maintained below shoulder height, earning a score of 1, while the lower arm remained in a neutral position between 60°–100°, resulting in a score of 1. The wrist was slightly deviated, giving a score of 2. When these values are cross-referenced in REBA Table B, the resulting Posture Score B is 2, indicating a very low ergonomic risk.

This posture confirms that the crane system allows the operator to work in a neutral, low-stress position, further validating the ergonomic effectiveness of the redesigned crane compared to manual lifting scenarios.

Score A (score from table A +load/force score)	Tabel C											
	Score B, (table B value +coupling score)											
	1	2	3	4	5	6	7	8	9	10	11	12
1	1	1	1	2	3	3	4	5	6	7	7	7
2	1	2	2	3	4	4	5	6	6	7	7	8
3	2	3	3	4	5	5	6	7	7	8	8	8
4	3	4	4	5	6	6	7	8	8	9	9	9
5	4	4	4	5	6	6	8	9	9	9	9	9
6	6	6	6	7	8	8	9	9	10	10	10	10
7	7	7	7	8	9	9	10	10	11	11	11	11
8	8	8	8	9	9	10	10	10	11	11	11	11
9	9	9	9	10	10	10	11	11	12	12	12	12
10	10	10	10	10	11	11	11	12	12	12	12	12
11	11	11	11	11	12	12	12	12	12	12	12	12
12	12	12	12	12	12	12	12	12	12	12	12	12

Figure 11. Group C Score REBA Worksheet Hydraulic Crane Fertilizer

In the fertilizer lifting process using the hydraulic crane, the operator maintained a highly ergonomic posture. The combined Posture Score A from trunk, neck, and leg positions was 1, and since the task involved no significant load stress (the operator only operates a lever), the Load/Force Score added was 0—thus keeping Score A = 1. From the upper limb assessment, Score B was calculated as 2, with no added coupling penalty, giving a Score B total of 2. By referencing Table C with Score A = 1 and Score B = 2, the resulting REBA Score C = 1. However,

due to repetitive actions (more than 4 per minute), an Activity Score of +1 was applied, bringing the Final REBA Score to 2.

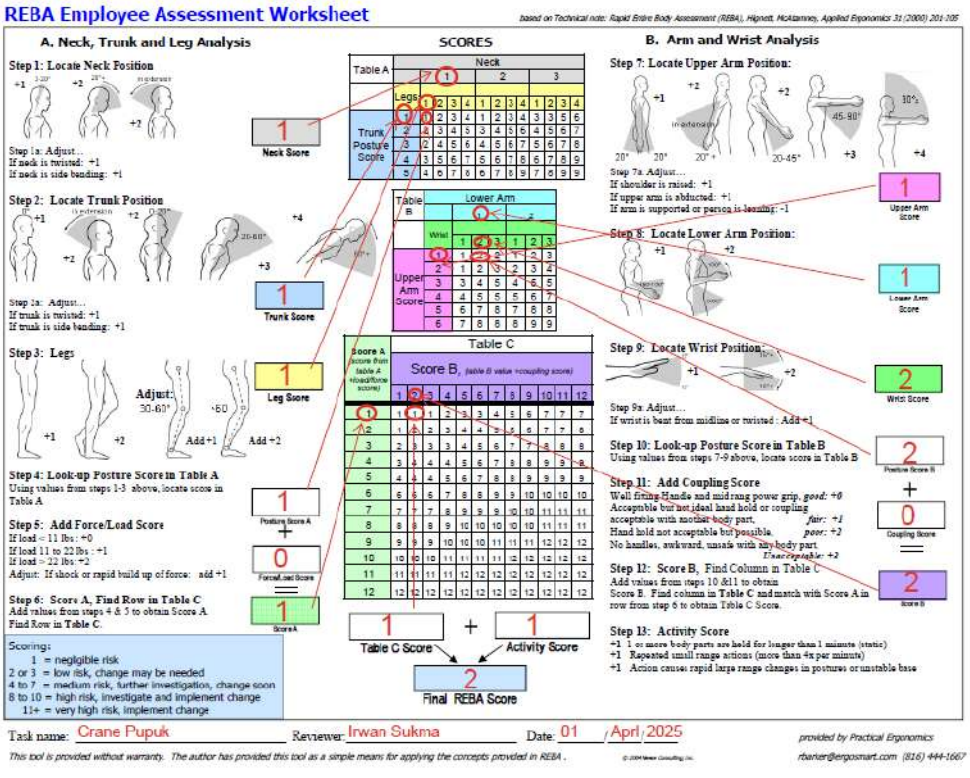

Figure 12. Complete REBA Worksheet Assessment Hydraulic Crane Fertilizer

This final score indicates a low ergonomic risk, meaning the system is safe to operate without requiring urgent ergonomic intervention. It demonstrates the success of the crane design in significantly improving operator safety and reducing musculoskeletal risk compared to manual lifting.

Ergonomic risk was assessed using the REBA (Rapid Entire Body Assessment) method. The analysis showed that the REBA score during manual lifting reached 12, classified as very high risk, requiring immediate corrective action. After implementation of the hydraulic crane, the REBA score dropped significantly to 2, indicating a low risk level that is acceptable. This reduction reflects a substantial improvement in ergonomic conditions and overall workplace safety.

3.5 Cost Production Hydraulic Crane Fertilizer

The implementation of an ergonomic lifting system on the Canycom S25A Fertilizer Spreader, a cost analysis was conducted to estimate the production expenses of the hydraulic crane unit. The analysis includes primary structural materials, hydraulic components, fabrication labor, and installation. The design utilizes readily available components such as SS400 carbon steel hollow pipes, hydraulic cylinders, and PTO-driven gear pumps, which are both cost-efficient and technically suitable for agricultural environments. The total cost estimate reflects small-batch or prototype-scale production in Indonesia and provides a practical basis for budgeting and scalability. Detailed cost components are presented in the following table.

Table 2. Cost Estimates Production

No.	Component / Material	Specification	Qty	Unit	Unit Cost (IDR)	Subtotal (IDR)
1	Hollow Carbon Steel SS400 Pipe	50×50×5 mm, total length ~4 m	4	m	250,000	1,000,000
2	Hydraulic Cylinder (Double Acting)	Ø25 mm bore, 300 mm stroke	2	pcs	1,200,000	2,400,000
3	Hydraulic Control Valve + Manual Lever	1 spool	1	unit	950,000	950,000
4	Hydraulic Hose + Fittings	High-pressure hose (3–4 m)	1	set	500,000	500,000
5	PTO Hydraulic Pump	Gear pump (10 MPa, 25 L/min)	1	unit	2,500,000	2,500,000
6	Hooks for Fertilizer Bags	Heavy-duty steel hooks	4	pcs	35,000	140,000
7	Mounting Brackets, Pins & Hinges	CNC cut & lathed	1	set	500,000	500,000
8	Welding & Fabrication Labor	MIG welding + assembly	1	ls	1,200,000	1,200,000
9	Painting & Finishing	Anti-corrosion industrial paint	1	ls	300,000	300,000
10	Testing & Installation	Load test, crane fitment	1	ls	250,000	250,000
	TOTAL ESTIMATED COST					**9,740,000**

4. Conclusions

This study successfully developed an ergonomic fertilizer lifting crane integrated with the Canycom S25A Fertilizer Spreader equipped with a 650-liter hopper. The crane design addresses the critical ergonomic challenges of manually lifting heavy fertilizer bags, which pose significant risks of musculoskeletal disorders. By utilizing a foldable two-segment hydraulic crane powered by the unit's PTO engine, the system enables efficient and safe lifting of four 50-kg bags simultaneously. Structural analysis confirmed that the crane operates safely under maximum loading conditions, with a safety factor above 1.5. Ergonomic evaluation using the REBA method showed a dramatic risk reduction—from a high-risk score of 12 during manual lifting to a low-risk score of 2 after implementing the crane system. The total estimated production cost for the hydraulic fertilizer lifting crane is approximately IDR 9,740,000, which includes structural materials, hydraulic components, labor, and installation. This cost is considered economical and feasible for small to medium-scale agricultural operations, particularly when compared to the long-term ergonomic benefits and reduced risk of musculoskeletal injuries among workers.

Acknowledgments: To finish this research and paper, the author would like to thank everyone who has contributed ideas and materials. Second, the author would like to express gratitude to Politeknik Negeri Jakarta's Mechanical Engineering Department's Design and Development Laboratory for providing the equipment used in this study. Third, in recognition of their time and efforts in sup-porting this research, the author thanks the waste material handling employees who will be pro-cessed.

References

1. C. Osha, C. Service, and E. Unit, "Ergonomic Guidelines for Manual Material Handling", [Online]. Available: https://www.cdc.gov/niosh/docs/2007-131/default.html
2. National Institute for Occupational Safety and Health, "Applications Manual for the Revised NIOSH Lifting Equation," 2021. [Online]. Available: https://stacks.cdc.gov/view/cdc/110725/cdc_110725_DS1.pdf
3. I. Ergonomic, *Ergonomic Check Point*. International Ergonomic Assosiation. [Online]. Available: https://www.ilo.org/sites/default/files/wcmsp5/groups/public/@ed_protect/@protrav/@safework/documents/instructionalmaterial/wcms_178593.pdf
4. K. K. E. Grandjean, *Fitting the Task to the Man: A Textbook of Occupational Ergonomics*. Taylor & Francis, 1988.
5. S. Pheasant and C. Haslegrave, *Bodyspace: Anthropometry, Ergonomics and the Design of Work*. 2018. doi: 10.1201/9781315375212.
6. Y. A. Pramana *et al.*, "Serambi Journal of Agricultural Technology (SJAT)," vol. 4, no. 1, pp. 46–54, 2022.
7. K. M. Clark, "Introduction to the Design of Mobile Hydraulic Systems - Part 1," no. 877, [Online]. Available: https://www.cedengineering.com/userfiles/Introduction to the Design of Mobile Hydraulic Systems - Part 1-R1.pdf
8. ISO 11228-1, "INTERNATIONAL STANDARD," vol. 2003, 2003.
9. enan J. E. P. Engineering, "CN217867646U Fertilizer Overhead Hoist in Bags," 2022 [Online]. Available: https://patents.google.com/patent/CN217867646U/en
10. M. Middlesworth, "A Step-by-Step Guide Rapid Entire Body Assessment (REBA)", [Online]. Available: https://ergo-plus.com/reba-assessment-tool-guide/
11. E. Plus, "RULA Employee Assessment Worksheet," vol. 24, no. 2, p. 1993, 1993.
12. M. S. Sanders and E. J. Mccormick, *Human Factors in Engineering and Design*. McGraw-Hili, Inc., 1993.

RiESTech
Recent in Engineering Science and Technology

MBI

Article

Red Roselle (Hibiscus sabdariffa L.) Tea as an Organic Corrosion Inhibitor for Low-Carbon Steel in 3.5% Sodium Chloride Solution

Giafin Bibsy Rahmaulita [1,*], Johny Wahyuadi Mudaryoto Soedarsono [1]

[1] Department of Metallurgical and Materials Engineering, Universitas Indonesia, Depok, Indonesia 16424
* Correspondence: giafinbibsy@gmail.com

Abstract: Corrosion of low-carbon steel in chloride media remains a persistent challenge across infrastructure and multiple industrial sectors. This study evaluates red roselle (*Hibiscus sabdariffa*) tea as a green corrosion inhibitor for low-carbon steel in a 3.5wt% NaCl using weight-loss measurements over 3, 6, 9, and 12 days, complemented by pH and corrosion-potential observations. A red roselle-tea concentration of 10 g/L with an additional 2 mL of liquid inhibitor was employed. Relative to the uninhibited control, mass-loss data show a measurable reduction in corrosion, with inhibition efficiency increasing from 8% at day 3 to a maximum of 16% at day 9; no further improvement was observed at day 12. The tea also stabilized solution pH and shifted the corrosion-potential toward more noble (less negative) values, consistent with formation of an adsorbed, partially blocking film attributed to polyphenolic constituents. Observed efficiencies are modest and toward the low end of reported values for plant-based inhibitors in neutral 3.5 wt% NaCl, underscoring the need to optimize extract loading, extraction/fractionation strategy, and test conditions. The results provide a quantitative benchmark for advancing roselle-derived green inhibitors.

Keywords: Low-carbon steel; Green Corrosion Inhibitor; Red Roselle Tea; Sodium Chloride; weight-loss method

Citation:. Rahmaulita, G. B., Soedarsono, J. W. M. (2025). Red Roselle (Hibiscus sabdariffa L.) Tea as an Organic Corrosion Inhibitor for Low-Carbon Steel in 3.5% Sodium Chloride Solution. Recent in Engineering Science and Technology, 3(04), 24–35. Retrieved from https://www.mbi-journals.com/index.php/ riestech/article/view/119

Academic Editor: Vika Rizka

Received: 20 June 2025
Accepted: 19 October 2025
Published: 31 October 2025

1. Introduction

Corrosion is a natural and inevitable process that leads to the deterioration of metals as a result of their interaction with the surrounding environment, often resulting in adverse consequences [1]. In everyday life, corrosion is commonly observed in buildings, infrastructure, and tools that utilize metals such as low carbon steel as primary materials. The destructive effects of corrosion have significant implications, not only compromising structural integrity and safety but also impacting environmental sustainability and economic stability [2].

One effective approach to reducing the rate of corrosion involves the use of corrosion inhibitors—substances that, when introduced in small quantities into a corrosive environment, can significantly slow down the degradation of metals [3]. Inorganic inhibitors, though widely used, often consist of hazardous chemical compounds that are costly and environmentally unfriendly. In contrast, organic inhibitors, particularly those derived from plant-based sources, offer a more sustainable and eco-friendly alternative to conventional chemical inhibitors.

The use of plant extracts as corrosion inhibitors has gained increasing attention due to their widespread availability, lower cost, and environmentally friendly nature [4–5]. These so-called green inhibitors are typically derived from various plant components, including flowers,

seeds, leaves, stems, and roots. Numerous studies have demonstrated the effectiveness of natural extracts in reducing corrosion rates. For example, research conducted by Elachi [6] reported corrosion inhibition efficiencies of 27.95% and 22.81% when using leaf and flower extracts of roselle on mild steel in a 0.5 M tetraoxosulfate solution. The study highlighted that roselle extracts exhibit greater effectiveness during the first 8 days of exposure. Similarly, Ameer observed that the inhibition efficiency increases with higher concentrations of the extract, with experiments involving the addition of red roselle extract to hydrochloric acid (HCl) solutions. Further research demonstrated that roselle extract achieved an inhibition efficiency of up to 97.59% when applied to a copper–zinc (Cu–Zn) alloy in a 1 M nitric acid (HNO_3) solution [7-8]. These findings underscore the significant potential of roselle as a green corrosion inhibitor across various metals and corrosive environments.

Dried red roselle flowers are rich in bioactive compounds such as flavonoids, polyphenolic acids, anthocyanins, sabdaretin, and hibiscetin. The characteristic red coloration of roselle, commonly referred to as hibiscus pigment, has been attributed to compounds including delphinidin, delphinidin-3-monoglucoside, and cyanidin-3-monoglucoside [8]. These constituents are known for their antioxidant properties, which contribute to their potential role as corrosion inhibitors.

The objective of this study is to evaluate the effectiveness of red roselle tea as a corrosion inhibitor for low carbon steel in a 3.5% sodium chloride solution. The investigation is based on varying immersion times to assess inhibition performance. Due to its high antioxidant content, red roselle tea is anticipated to reduce the corrosion rate by forming a protective layer on the metal surface.

2. Materials and Experiment Methods

Immersion testing and post-exposure cleaning followed ASTM G31 and ASTM G1, respectively, to ensure reproducibility. Weight-loss measurements are complemented by pH tracking and corrosion-potential observations, with results reported from replicate trials. Figure 1 provides an overview of the experimental workflow to facilitate replication.

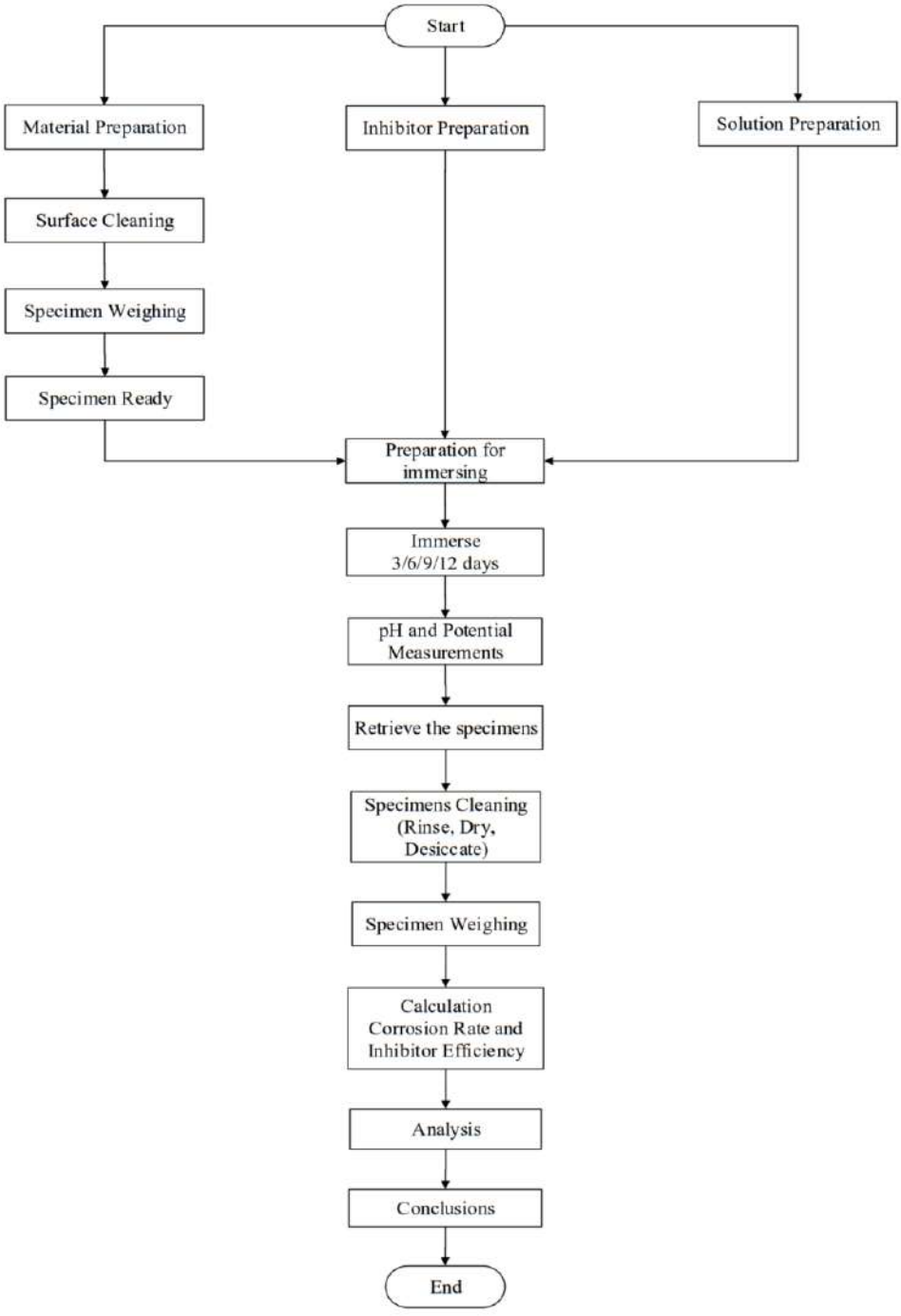

Figure 1. Experimental workflow integrating preparation, immersion, monitoring (pH, corrosion potential), post-exposure cleaning, and corrosion rate for low-carbon steel in 3.5 wt% NaCl.

2.1 Sample and Environment Preparation

The materials that will be used are low carbon steel. The sheets of low carbon steel are 1mm thick and cut into 24 sheets with measurements of 25mm x 20mm x 1mm. The top of the samples that have been cut are drilled into to create holes that each have a diameter of 3mm for the hanging of a sample in accordance with Figure 2. After, the sample was sanded starting with 80 grit to 240 grit sandpaper to remove oxides on the surface of the sample. Each sample was then weighed using a digital scale.

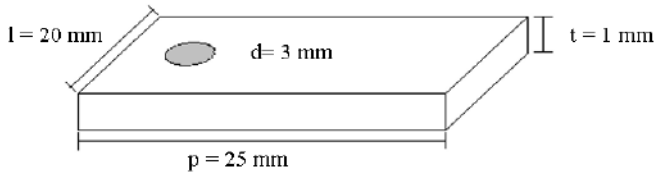

Figure 2. Illustrates the sample of the experiment

The solution that used is a solution of sodium chloride with a concentration of 3.5%, used as a simulation of sea water. To make the solution, dissolve 35 grams of Sodium chloride within 1 liter of distilled water. Based on ASTM G31-72, the volume of solution that can be found using the maximal ratio is 0.4 from the area of the surface of the sample.

Area of the surface of the sample:

$= (2 \times p \times l) + (2 \times p \times t) + (2 \times l \times t) - ((2\pi r^2) + (t \times 2\pi r))$

$= (2 \times 25 \times 20) + (2 \times 25 \times 1) + (2 \times 20 \times 1) - (2 \times 3{,}14 \times 1{,}52) + (1 \times 2 \times 3{,}14 \times 1{,}5)$

$= 1085{,}29\ mm^2$

Minimum volume = 0,4 x 1085,29 = 434,119 ml ≈ 450 ml

2.2 Inhibitor Preparation

The concentration of the inhibitor that will be used is 10 gpl. The method used will be inserting 1 gram of dry Rosela flowers into a glass beaker, then, adding 100 ml of distilled water, heating, then stirring with a magnetic stirrer to distill the flowers so that we produce a mixture of Rosela with a concentration of 10 gpl. strain the dregs out, wait until the mixture is cold then use the inhibitor as in Figure 3.

Figure 3. Roselle Tea as inhibitor

2.3 Soak Test

The prepared sample is then hanged with string then dipped into a plastic vessel that has been filled with the sodium chloride 3.5% solution ±450 ml at room temperature. Each sample is then dipped into 1 vessel. To ease the observation and research process, each vessel has been given a number and different treatment. The sample will be dipped into the solution of Sodium chloride without an inhibitor and with an addtional 2 ml added over 3, 6, 9 and 12 days.

After immersing the samples, each vessel had their metal potential measured. A multimeter was used to measure the metal potential, where each positive side is connected with the

sample and the negative side with standard electrodes Ag/AgCl. The final potential of each vessel was measured before raising the samples.

2.4 Calculations of Corrosion Rate and Inhibitor Efficiency

The corrosion rate in this study was determined using the mass loss method, which involves measuring the reduction in mass of the metal specimens due to corrosion. Initially, each sample was accurately weighed and subsequently immersed in the test solution for a specified duration. Upon completion of the immersion period, the samples were retrieved, cleaned to remove corrosion products, and reweighed. The difference between the initial and final weights represents the mass loss attributable to corrosion. This mass loss is then used to calculate the corrosion rate by considering the exposed surface area of the specimen, the duration of immersion, and the material density. The corrosion rate was computed using the standard formula, and the corresponding units and constants are presented in Table 1. The corrosion rate can be done with the following equation 1:

$$Corrosion\ Rate\ (MPY) = \frac{K.W}{D.A.T} \quad (1)$$

Where: K = constant (Table 2)
W = mass loss (gr)
D = mass type (gr/cm3)
A = surface area of immersed (cm2)
T = time (hours)

Table 1. Units of the corrosion rate with the constant K [1]

Corrosion Rate Units Desired	Constant (*K*) in Corrosion Rate Equation
mils per year (mpy)	3.45×10^6
inches per year (ipy)	3.45×10^3
inches per month (ipm)	2.87×10^2
millimetres per year (mm/y)	8.76×10^4
micrometres per year (um/y)	8.76×10^7
picometres per second (pm/s)	2.78×10^6
grams per square meter per hour (g/m^2·h)	$1.00 \times 10^4 \times D$
milligrams per square decimeter per day (mdd)	$2.40 \times 10^6 \times D$
micrograms per square meter per second (µg/m^2·s)	$2.78 \times 10^6 \times D$

The efficiency of the inhibitor shows that the percentage of the decline of corrosion rate with the addition of inhibitor can be compared with the corrosion rate without any additions to the inhibitor. The larger the efficiency of the enhibitor, the better the obstruction of the corrosion rate. Calculating the efficiency of the inhibitor using equation 2.

$$Inhibitor\ Efficiency = \frac{X_a - X_b}{X_a}\ x\ 100\% \quad (2)$$

Where: Xa = corrosion rate without inhibitor
Xb = corrosion rate with the addition of an inhibitor

3. Results and Discussion

3.1 Material Characterization Results

The sample has been tested at the Center for Material Processing and Failiure Analysis (CMPFA) using an Optical Emission Spectrometer. The results conclude that the composition of low carbon steel are as in Table 2. Based on the results in Table 2, the Optical Emission Spectroscopy (OES) analysis shows that the carbon steel used has a carbon content (C) of 0.057%, classifying it as low-carbon steel.

Table 2. Composition of the low carbon steel used

C (%)	Si (%)	S (%)	P (%)	Mn (%)	Ni (%)	Cr (%)
0.057	0.007	0.003	0.007	0.160	0.031	0.023
Mo (%)	**Ti (%)**	**Cu (%)**	**Nb (%)**	**V (%)**	**Pb (%)**	**Fe (%)**
<0.005[2]	<0.002[2]	0.121	<0.002[2]	<0.002[2]	<0.025[2]	Bal.

3.2 Visual Observation Results

Figures 4 and 5 illustrate the initial condition of the low carbon steel specimens prior to immersion in solutions with and without the added inhibitor. The surfaces originally exhibited a uniform gray oxide layer, covering the entire sample. To eliminate this oxidation and ensure a clean, reactive surface, the specimens were mechanically polished using a series of abrasive papers with grit sizes 80, 100, 150, and 240. This surface preparation was essential to standardize the initial condition of all samples before exposure to the test solutions.

a) **(b)** **(c)** **(d)**

Figure 4. Low-carbon steel coupons were assigned immersion durations are **(a)** 3, **(b)** 6, **(c)** 9, **(d)** 12 days in 3.5 wt% NaCl without inhibitor

a) **(b)** **(c)** **(d)**

Figure 5. Specimen assignment for the roselle-inhibited condition **(a)** 3, **(b)** 6, **(c)** 9, **(d**) 12 days

After the immersion of 3, 6, 9, and 12 days, the sample which was submerged in the solution without an added inhibitor was raised and visually observed, the results can be seen in Figure 6. It can be seen that almost the entire surface of the sample has uniformly corroded. This uniform corrosion can be seen by the scale of yellow-reddish colors that has cover the

entire surface of the sample. The more time spent immersed, the more the scale will form. When pickled this scale can be cleaned easily but, it leaves marks and stains on the entirety of the surface of the metal which has been covered by the scale. The results of the visual observation after cleaning or pickling can be seen in Figure 7.

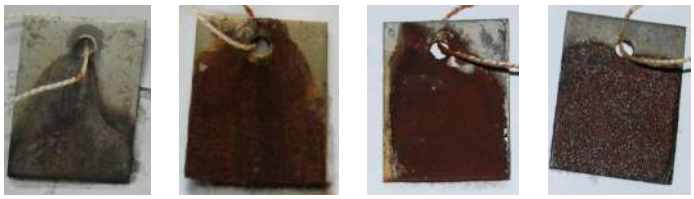

a) **(b)** **(c)** **(d)**

Figure 6. Uninhibited exposure, post-immersion appearance. Representative coupon surfaces after **(a)** 3, **(b)** 6, **(c)** 9, **(d)** and 12 days in 3.5 wt% NaCl, showing progressive accumulation of corrosion products

a) **(b)** **(c)** **(d)**

Figure 7. Uninhibited exposure, post cleaning surfaces. Representative coupons previously immersed for **(a)** 3, **(b)** 6, **(c)** 9, **(d)** 12 days in 3.5 wt% NaCl; images recorded after ASTM G1 cleaning reveal the underlying substrate following rust removal.

The sample with an added inhibitor's results can be seen in Figure 8. On the sample, the scale has a darker red coloration. But, the scale that covers the sample that was immersed in the solution with an added inhibitor has spread less and is not as thick when juxtaposed with the one without an added inhibitor. when pickled, the scale that has formed was more difficult to clean. Results of the visual observation after cleaning or pickling can be seen in Figure 9.

a) **(b)** **(c)** **(d)**

Figure 8. Inhibited, post-immersion surfaces. Representative coupons after **(a)** 3, **(b)** 6, **(c)** 9, **(d)** 12 days in 3.5 wt% NaCl, showing reduced corrosion-product coverage relative to the uninhibited

a) **(b)** **(c)** **(d)**

Figure 9. Inhibited, post-cleaning surfaces. Representative coupons previously immersed for **a)** 3, **(b)** 6, **(c)** 9, **(d)** 12 days in 3.5 wt% NaCl, images taken after ASTM G1 cleaning reveal the underlying substrate, indicating improved surface preservation relative to the uninhibited

3.2 Effects on pH and Corrosion Potential

The addition of the inhibitor led to an increase in the solution's alkalinity, suggesting that red roselle tea contributes to reducing the corrosiveness of the environment. This alteration indicates a stabilizing influence on the electrochemical conditions within the 3.5% sodium chloride solution. The observed pH differences between the inhibited and uninhibited systems are mainly attributed to the oxygen reduction reaction at cathodic sites. The pH change is illustrated in Figure 10a, representing the condition before immersion, and Figure 10b, reflecting the condition after immersion. The dominant cathodic reaction in such chloride-containing environments is expressed as:

$$\text{Oxygen reduction reaction:} \quad O_2 + 2H_2O + 4e \rightarrow 4OH^- \quad [1]$$

The oxygen reduction reaction results in the formation of hydroxide ions (OH^-), which contributes to an increase in the basicity of the environment. In systems containing organic inhibitors, such as red roselle extract, an oxygen scavenging mechanism is often observed. This mechanism reduces the availability of dissolved oxygen, thereby limiting the extent of the oxygen reduction reaction. As a consequence, the formation of OH^- is diminished, resulting in a more moderate increase in pH in the solution containing the inhibitor compared to the uninhibited system.

The measurement of corrosion potential showed a positive shift from –0.625 V to –0.572 V (vs. Ag/AgCl), indicating improved protection of the low carbon steel surface. Both the inhibited and uninhibited solutions were tested using a standard Ag/AgCl reference electrode. The potential changes are illustrated in Figure 11a, representing the condition prior to immersion, and Figure 11b, depicting the condition after the immersion period. The resulting potential values were averaged and then converted to the standard hydrogen electrode (SHE) scale using Equation (3):

$$Potential\ (V) vs\ SHE = potential\ (V) vs\ Ag/AgCl\ + 0{,}222V \qquad (3)$$

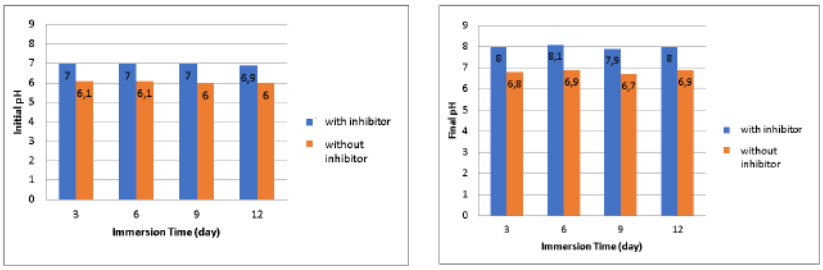

a) **(b)**

Figure 10. pH during immersion in 3.5 wt% NaCl. **(a)** Initial pH; **(b)** final pH at the end of each exposure (3, 6, 9, 12 d). Bars compare no inhibitor and roselle-inhibited conditions. The inhibited condition holds a higher, near-neutral to mildly alkaline than the unhibited, indicating pH stabilization consistent with inhibitor adsorption and weak buffering by the inhibitor

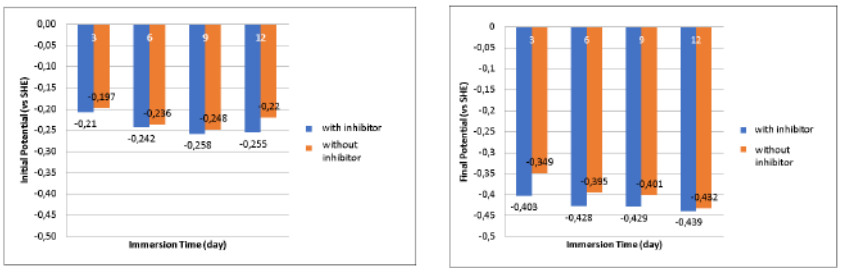

a) **(b)**

Figure 11. Corrosion potential during immersion in 3.5 wt% NaCl, reported vs SHE. **(a)** Initial; **(b)** final corrosion potential at the end of each exposure (3, 6, 9, 12 d). The inhibited condition shows a positive shift toward more noble potentials relative to the uninhibited.

3.3 Effects of Immersion Testing Period on the Weight Reduction of Metal, Corrosion Rate and Inhibitor Efficiency

Immersion tests at 3, 6, 9, and 12 days show clear time dependence: cumulative mass loss increases with exposure under both conditions but remains consistently lower when roselle tea is present, showed in Figure 12. Corrosion rates calculated from the weight-loss data follow this pattern. In the uninhibited condition, the rate evolves from 7.62 to 7.88 to 6.17 to 5.91 mpy (days 3→6→9→12), while the inhibited condition shows 7.02 to 6.68 to 5.17 to 5.19 mpy over the same interval. The minor rise at day 6 in the uninhibited condition and the slight uptick at day 12 in the inhibited case are typical early and late-stage transients superimposed on an overall downward trend. Inhibition efficiency mirrors this evolution, increasing from 7.93% (day 3) to 15.19% (day 6) and peaking at 16.08% (day 9) before easing to 12.28% (day 12), showed in Figure 13.

The time evolution of these metrics points to adsorption-controlled protection. At short times, a freshly prepared steel surface presents abundant active sites, so both anodic iron dissolution and the paired cathodic reaction proceed readily. As immersion continues, two coupled barriers develop at the interface. First, corrosion products accumulate and increase diffusion resistance to reactants. Second, organic constituents of the roselle tea adsorb on the

metal, occupying catalytic sites and forming a thin organic layer. The combined effect is a reduction of effective interfacial area and a slowdown of charge transfer, which explains the steady decrease in corrosion rate across the 12-day window and the consistently lower values in the inhibited condition.

The efficiency profile, rising through day 9 and moderating by day 12, further supports this mechanism. Early in exposure, surface coverage grows toward a compact, Langmuir-like monolayer as inhibitor molecules compete successfully for adsorption sites, yielding a marked improvement in protection, reflected in the increase from ~8% to ~16% efficiency between days 3 and 9. With longer exposure, partial desorption, rearrangement of the organic layer, or competitive penetration by chloride and dissolved oxygen can reduce the integrity of the protective film. In parallel, the corrosion-product layer may evolve toward a more porous or cracked morphology under sustained attack. Either pathway slightly diminishes the overall barrier, which is consistent with the modest loss of efficiency observed at day 12 alongside the small rate increase in the inhibited condition.

Apparent anomalies in the rate profile have a straightforward mechanistic basis. The day-6 rise in the uninhibited likely reflects the high reactivity of a freshly revealed steel surface together with a corrosion film that is still thin and discontinuous, as that film thickens and coalesces, the rate declines again by days 9 and 12. Likewise, the slight day-12 increase under inhibition is consistent with a modest shift in adsorption–desorption balance or the emergence of local defects within the mixed organic/corrosion-product layer, briefly exposing small areas of bare metal to the NaCl electrolyte.

In NaCl solution, the roselle tea suppresses metal dissolution across 3–12 days, with maximal effect at mid-exposure when the mixed organic/corrosion-product film is most compact and uniform. The modest late-stage attenuation is best attributed to interfacial reorganization partial desorption and the development of porosity rather than any change in the underlying electrochemical pathway. The convergent signatures time monotonic growth of mass loss, systematically lower corrosion rates in inhibited condition, and an efficiency profile that peaks before gently declining, are consistent with an adsorption-controlled inhibition mechanism for *Hibiscus sabdariffa* under the conditions studied.

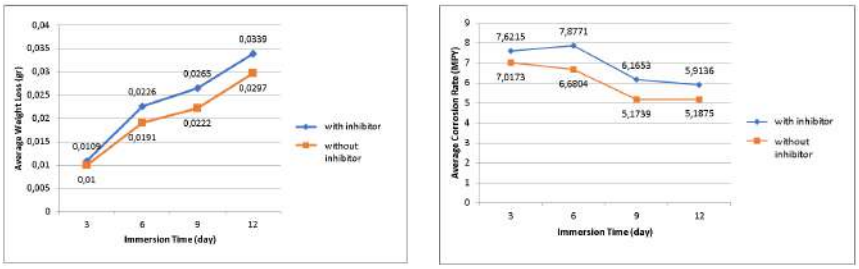

a) **(b)**

Figure 12. Mass loss **(a)** and corrosion rate **(b)**, versus immersion time (3, 6, 9, 12 d) in 3.5 wt% NaCl. Trends indicate progressive mass loss and a parallel decrease in CR; inhibition remains weak to moderate, maximizes near 9 days diminishing thereafter.

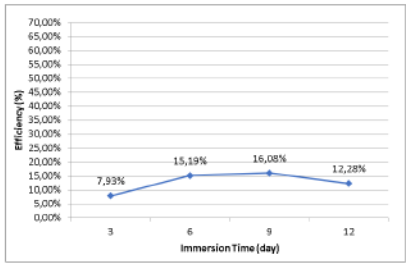

Figure 13. Weight loss based inhibition efficiency, η (%), versus immersion time in 3.5 wt% NaCl (roselle-inhibited condition). Efficiency rises from ~8% (3 days) to a maximum ~16% (9 days) and then declines to ~12% (12 days), indicating modest, time-dependent mitigation.

4. Conclusion

Roselle (*Hibiscus sabdariffa* L.) tea gives modest protection of low-carbon steel in 3.5 wt% NaCl. Weight-loss inhibition efficiency rises from ~8% (3 days) to ~15% (6 days), peaks near ~16% (9 days), then slips to ~12% (12 days). As expected, cumulative mass loss increases with time, while the instantaneous corrosion rate falls in both uninhibited and inhibited condition and stays lower with the extract. A slightly higher, more stable pH and a nobler potential under inhibition point to a partially blocking adsorbed/oxide film and a mixed-type inhibition behavior.

Performance and mechanistic clarity remain priorities. Subsequent studies should define the dose–response and persistence beyond 12 days; re-evalute the extraction by replacing brewed tea with a crude, non-thermal roselle flower extract that preserves thermolabile antioxidants (e.g., cold/hydroalcoholic extraction ≤40 °C); fractionate and quantify phenolics, correlating composition with inhibition efficiency (η); incorporate Tafel polarization to obtain $i_{(corr)}$ and resolve anodic/cathodic contributions; and verify film/rust chemistry via SEM/EDS, FTIR/ATR, and XRD. Sensitivity studies across temperature, pH, salinity, and hydrodynamics, together with benchmarking against a commercial green inhibitor under identical conditions, will define the practical operating window. Report replicate statistics (e.g., means with 95% confidence intervals) to convey effect size. These findings establish a quantitative baseline for advancing roselle-derived, environmentally benign inhibitors in chloride media.

Acknowledgments: The comments and suggestions from all the editors and reviewers are very much appreciated.

Conflicts of Interest: The authors declare no conflict of interest.

References

1. M. S. Sanders and E. J. Mccormick, *Human Factors in Engineering and Design*. McGraw-Hili, Inc., 1993. Fontana, G. 1986. *Corrosion Engineering*. New York: McGraw-Hill.
2. Asdim. 2008. "Penghambatan reaksi korosi baja dengan menggunakan ekstrak kulit buah manggis (*Garcinia mangostana* L.) sebagai inhibitor dalam larutan garam." Undergraduate thesis, Jurusan Kimia, Fakultas MIPA, Universitas Bengkulu.
3. Ilim, dan Beni Hermawan. 2008. "Studi penggunaan ekstrak buah lada (*Piper nigrum* Linn), buah pinang (*Areca catechu* Linn), dan daun teh (*Camellia sinensis* L. Kuntze) sebagai inhibitor korosi baja lunak dalam condition air laut buatan yang jenuh gas CO_2." Undergraduate thesis, Jurusan Kimia, FMIPA, Universitas Lampung.
4. Okafor, P. C., V. I. Osabor, and E. E. Ebenso. 2007. "Eco-friendly corrosion inhibitors: Inhibitive action of ethanol extracts of *Garcinia kola* for the corrosion of mild steel in H_2SO_4 solution." *Pigment and Resin Technology* 36: 299–305.
5. Rajendran, S., A. J. Amalray, M. J. Joice, N. Anthony, D. C. Trived, and M. Sundaravadivelu. 2004. "Corrosion inhibition by the caffeine-Zn system." *Corrosion Reviews* 22: 233–48.
6. Elachi, Emmanuel E., and Austine Justine. 2022. "Corrosion inhibition potentials of roselle (*Hibiscus sabdariffa*) in tetraoxosulphate(VI) acid solution." *International Journal of Engineering and Applied Physics* 2 (3).
7. Ameer. 2015. "Corrosion inhibition by naturally occurring *Hibiscus sabdariffa* plant extract on a mild steel alloy in HCl solution." *Turkish Journal of Chemistry*.
8. Seham, Shahen. 2022. "Eco-friendly roselle (*Hibiscus sabdariffa*) leaf extract as natural corrosion inhibitor for Cu–Zn alloy in 1 M HNO_3." *Egyptian Journal of Chemistry*.
9. Murthy, Z. V. P., and Vijayaragavan. 2021. "Mild steel corrosion inhibition by acid extract of leaves of *Hibiscus sabdariffa* as a green corrosion inhibitor and sorption behavior." *Green Chemistry Letters and Reviews*.
10. Okta, Malinda, dan Syakdani. 2021. "Pengujian berbagai aktivitas ekstrak air rosella secara *in vitro* (*Hibiscus sabdariffa* L.)." *Jurnal Kinetika* (Politeknik Negeri Sriwijaya).
11. Ahmed, A., and Al-Mashhadani. 2020. "Inhibition corrosion: Mechanisms and classifications—an overview." *Al-Qadisiyah Journal of Pure Science*.
12. Verma, Chandrabhan, and Akram Alfantazi. 2023. "Are extracts really green substitutes for traditional toxic corrosion inhibitors? Challenges beyond origin and availability." *Sustainable Chemistry and Pharmacy*.
13. Kaban, Agus Paul Setiawan, Wahyu Mayangsari, Mochammad Syaiful Anwar, Ahmad Maksum, Rini Riasutti, Taufik Adityawarman, and Johny Wahyuadi Soedarsono. 2022. "Experimental and modelling waste rice husk ash as a novel green corrosion inhibitor under acidic environment." *Materials Today: Proceedings* 62: 4225–34.
14. Soedarsono, Johny Wahyuadi, Muhammad Nafies Shihab, Muhammad Fikri Azmi, and Ahmad Maksum. 2018. "Study of *Curcuma xanthorrhiza* extract as green inhibitor for API 5L X42 steel in 1 M HCl solution." *IOP Conference Series: Earth and Environmental Science* 105 (1): 012060.

RiESTech
Recent in Engineering Science and Technology

MBI

Article

Influence of Moringa Leaf and Purple Sweet Potato Extract Concentrations on the Inhibition Efficiency of API 5L Steel in Acidic Medium

Yudha Pratesa [1,*], Kezia [1], Tio Angger Pertama [1], Johny Wahyuadi Soedarsono [1]

[1] Department of Metallurgical and Materials Engineering, Universitas Indonesia, Depok, Indonesia 16424
* Correspondence: yudhapratesa@ui.ac.id

Abstract: This study aimed to investigate the corrosion inhibition mechanism of moringa leaves extract (Moringa oleifera) and purple sweet potato extract (Ipomoea batatas) extract as environmentally friendly inhibitors for low carbon API 5L steel in a 0.2 M HCl solution. Potentiodynamic polarization and electrochemical impedance spectroscopy (EIS) tests were conducted with varying concentrations and combinations of the two inhibitors to evaluate their corrosion inhibition performance. The results indicated that both inhibitors individually function effectively as green corrosion inhibitors. However, their combination did not offer adequate protection for API 5L steel in a 0.2 M HCl environment. FTIR analysis of the inhibitors confirmed the presence of flavonoid compounds in both extracts. Potentiodynamic polarization tests showed that increasing the concentration of moringa leaves extract resulted in a decrease in the corrosion rate and an increase in %IE, with the highest efficiency reaching 73.08%. Similarly, an increase in the volume of purple sweet potato extract also resulted in a reduced corrosion rate, with a maximum inhibition efficiency of 65.31%. However, the combination of both inhibitors led to an increase in the corrosion rate. The results of the EIS test demonstrated that both inhibitors protect the metal by forming a protective film layer on its surface. The adsorption behavior of the inhibitors corresponds to a physical adsorption process and aligns with the Langmuir adsorption isotherm model.

Keywords: Moringa leaves; Purple sweet potato; FTIR; Potentiodynamic polarization; EIS

Citation: Pratesa, Y., Kezia, Pertama, T. A., Soedarsono, J. W. (2025). Influence of Moringa Leaf and Purple Sweet Potato Extract Concentrations on the Inhibition Efficiency of API 5L Steel in Acidic Medium. Recent in Engineering Science and Technology, 3(04), 36–48. Retrieved from https://www.mbi-journals.com/index.php/riestech/article/view/120

Academic Editor: Vika Rizka

Received: 22 June 2025
Accepted: 6 September 2025
Published: 31 October 2025

1. Introduction

Corrosion is the detrimental outcome of a chemical reaction between a metal or alloy and its surrounding environment [1]. It poses a significant challenge and is commonly encountered across various industrial sectors. The corrosion problems will decrease the quality of equipment or facilities that may affect the final product and work safety. One method that can be done to control corrosion in ferrous materials such as steel is to use corrosion inhibitors. Corrosion inhibitors are compounds added to environments with small concentrations that can decrease corrosion rates in metals [2]. Nowadays the concern for the environment is increasing, this affects the selection of inhibitors. Green corrosion inhibitors are optional because they are non-toxic, biodegradable, safe for human and environment.

Green corrosion inhibitors are made from plant and grain extracts. Plant extracts such as skin, leaves and stems may inhibit the corrosion rate because it contains heterocyclic compounds such as alkaloids, flavonoids, nicotine, hydrazine, alanine, quinolone, aniline, pyridine

and others. In this study, extracts from moringa leaves (Moringa oleifera) and purple sweet potato (Ipomoea batatas) were used as green corrosion inhibitors.

Moringa oleifera or Kelor in Bahasa Indonesia is belong to Moringaceae family that is distributed mostly in tropical and subtropical regions. Moringa products, from leaves, flowers to seeds, contain a number of macronutrients that are known to be good for the health of the body. In addition, moringa leaves contain antioxidants such as tannins, triterpenoid steroids, flavonoids, saponins, anthraquinones, and alkaloids [3]. This conditions makes kelor potential to be used as green corrosion inhibitor. Research done by Subasree et al. found that moringa leaves can be used as green corrosion inhibitor for low carbon steel in 1M H2SO4 [4]. The inhibition efficiency (IE) increased with increasing extract concentration, IE 96% was observed with 8 ml of plant extract in acidic media.

Purple sweet potato (Ipomoea batatas) is well known for its antioxidant content. It is called 'purple' due to the characteristic color of the tuber and belongs to the Convolvulaceae family. The antioxidant properties of purple sweet potato are largely attributed to anthocyanins. Anthocyanins are key compounds in purple sweet potatoes, derived from a monoaromatic structure known as cyanidin. Anthocyanins are derived from cyanidin, either through the addition or removal of hydroxyl groups or by methylation. Anthocyanins are also recognized for their antioxidant properties. A study conducted by Ayende et al. found that purple sweet potato extract can reduce the corrosion rate of API 5L steel in produced water [5].

This research is done to see the inhibition mechanism of moringa, purple sweet potato and combination between moringa and purple sweet potato.

2. Materials and Experiment Methods

2.1. Preparation of the test solution

The test solution used in this study was 0.2 M HCl. It prepared from 864 ml of 37% HCl and dissolved in 136 ml distilled water. Two types of inhibitors were used: moringa leaf extract and purple sweet potato extract, each at concentrations of 0, 1000, 2000, 3000, 4000, and 5000 ppm. In addition, purple sweet potato extract at various concentrations was combined with moringa leaf extract at a fixed concentration of 5000 ppm.

2.2. Specimen preparation

This study used API 5L with chemical composition was as follows (wt%): 0.193% C, 0.309% Si, 0.404% Mn, 0.013% P, 0.012% S, 0.024 Cr, 0.027% Mo, 0.035% Ni, 0.008% Al, 0.119% Cu, 0.004% Nb, 0.004% Ti, 0.007% V and Fe balance. It was tested with using Optical Emission Spectroscopy (OES). The specimen was 10 mm in diameter exposed surface area and mounted using epoxy resin. The exposed area was wet polished with 200, 400 and 600 SiC paper until previous coarse scratch by sectioning are removed, then it was rinsed with distilled water and dried. This process was repeated in every potentiodynamic testing.

2.3. Electrochemical measurement

A conventional three-electrode cell was used for all electrochemical measurements. The API 5L specimen served as the working electrode, with a platinum sheet as the counter electrode. The cell potential was measured against a saturated calomel electrode (SCE) as the reference. The working electrode was prepared in the form of a cylindrical API 5L rod, embedded in araldite, with an exposed bottom surface area of 0.785 cm² in contact with 500 mL of 0.2 M HCl electrolyte.

Potentiodynamic experiments were conducted at a scan rate of 1 mV/s, with a scan range from -1 V to +2 V relative to the open circuit potential (OCP). Tafel curves were extrapolated to the corrosion potential to calculate the electrochemical kinetic parameters. The IE were obtained by using Equation (1):

$$IE = \left[1 - \left(\frac{i_{corr\,(i)}}{i_{corr\,(o)}}\right)\right] x\ 100\% \quad (1)$$

where icorr (o) and i corr (i) represent the corrosion current densities of the specimen in the absence and presence of various concentrations of the inhibitor, respectively.

EIS measurements were conducted to determine the polarization resistance (Rct) and double layer capacitance (Cdl). The study was carried out using a potential amplitude of 10 mV, with a frequency range from 10 kHz to 0.1 Hz. The inhibition efficiency (IE) was calculated using Equation (2):

$$IE = \left[1 - \left(\frac{R_{ct\,(i)}}{R_{ct\,(o)}}\right)\right] x\ 100\% \quad (2)$$

where Rct (o) and Rct (i) represent the charge transfer resistance of the specimen in the absence and presence of the inhibitors, respectively.

2.4. Fourier Transform Infrared (FTIR) testing

FTIR testing was conducted to identify the types of functional groups present in the organic compounds, such as alcohols, alkaloids, and free elements containing nitrogen (N), oxygen (O), phosphorus (P), and sulfur (S).

3. Results and Discussion

3.1. Potentiodynamic Polarization

Tafel plots of the API 5L electrode in 0.2 M HCl solution with varying concentrations of moringa leaf extract, purple sweet potato extract, and their combination are presented in Figure 1.

The electrochemical parameters, i.e., corrosion potential (Ecorr), corrosion current density (icorr), anodic (βa) and cathodic (βc) slopes shown in Table 1-3, were collected from tafel plots and polarization resistance experiments carried out separately. Table 1 shows that the value of Ecorr has changed in both positive and negative directions, which means that anodic dissolution of metals and cathodic reduction of hydrogen ions have decreased due to the adsorption of moringa extract on the anodic and cathodic parts of the metal surface.

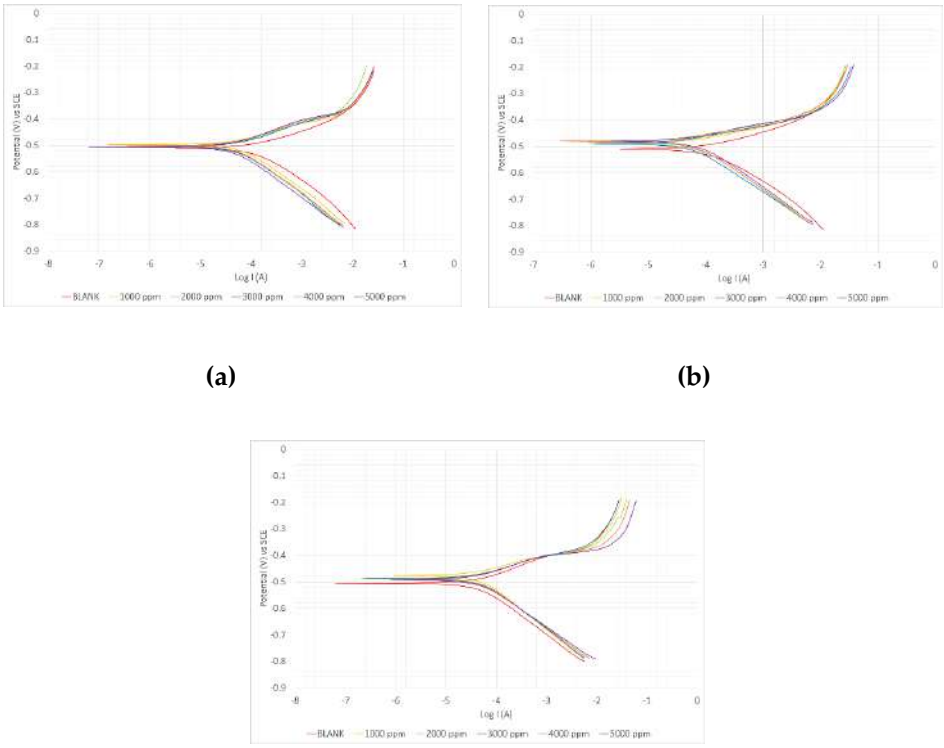

Figure. 1. Polarization curves of API 5L in different inhibitor concentration **(a)** Moringa leaves extract; **(b)** Purple sweet potato extract; **(c)** Combination of both.

In other words, these inhibitors belong to the mixed-type inhibitor category [6]. Changes in the value of Ecorr with and without the addition of inhibitors greater than 85 mV in either the anodic or cathodic direction indicate that the inhibitors belong to the anodic or cathodic inhibitor type. However, if the change in Ecorr between the absence and presence of inhibitors is less than 85 mV, the inhibitors are classified as mixed-type inhibitors [7]. This study showed a maximum change in Ecorr of 19 mV, indicating that Moringa extract belong to the mixed-type inhibitor category. This finding is further supported by research conducted by Fouda et al., who reported a maximum Ecorr shift of 48 mV when using moringa leaves extract as an inhibitor in 2 M HCl [16].

The value of icorr also with increasing inhibitor concentration due to a larger surface area of the electrode being covered by the inhibitors. This phenomenon contributes to a reduction in the corrosion rate. Additionally, decreases in the values of βc and βa are observed with increasing inhibitor concentration, indicating that both the anodic dissolution of metals and cathodic reduction of hydrogen ions have been suppressed due to the adsorption of Moringa leaves extract inhibitors on the anodic and cathodic regions of the steel surface [8].

Table 2 shows the electrochemical parameters for API 5L in the absence and presence of purple sweet potato extract. A maximum change in Ecorr by 31 mV indicates that purple sweet potato extract inhibitors belong mixed inhibitor type. A similar conclusion was also drawn from the application of purple sweet potato extract in a 3.5% NaCl environment [17].

Table 1. Electrochemical parameters for API 5L in moringa leaves extract inhibitor.

C (ppm)	E_{corr} (mV vs SCE)	i_{corr} (μA/cm²)	β_c (mV/dec)	β_a (mV/dec)	CR (mpy)	%EI
0	-511	211,00	$1,73 \times 10^{3}$	$1,25 \times 10^{-3}$	123	0,00
1000	-492	89,30	$1,61 \times 10^{3}$	$1,06 \times 10^{-3}$	52,02	57,68
2000	-505	86,10	$1,68 \times 10^{3}$	$1,18 \times 10^{-3}$	50,20	59,19
3000	-506	86,30	$1,71 \times 10^{3}$	$1,08 \times 10^{-3}$	50,31	59,10
4000	-502	78,30	$1,64 \times 10^{3}$	$1,06 \times 10^{-3}$	45,64	62,89
5000	-506	56,80	$1,55 \times 10^{3}$	$1,02 \times 10^{-3}$	33,13	73,08

Table 2. Electrochemical parameters for API 5L in purple sweet potato inhibitor.

C (ppm)	E_{corr} (mV vs SCE)	i_{corr} (μA/cm²)	β_c (mV/dec)	β_a (mV/dec)	CR (mpy)	%EI
0	-511	211,00	$1,73 \times 10^{3}$	$1,25 \times 10^{-3}$	123	0,00
1000	-490	114,00	$1,80 \times 10^{3}$	$1,07 \times 10^{-3}$	66,51	45,97
2000	-488	103,00	$1,74 \times 10^{3}$	$1,09 \times 10^{-3}$	60,25	51,18
3000	-489	73,20	$1,60 \times 10^{3}$	$9,91 \times 10^{-3}$	42,69	65,31
4000	-481	88,20	$1,73 \times 10^{3}$	$1,04 \times 10^{-3}$	51,38	58,20
5000	-480	109,00	$1,77 \times 10^{3}$	$1,03 \times 10^{-3}$	63,51	48,34

Table 3. Electrochemical parameters for API 5L in combination of both inhibitors.

C (ppm)		E_{corr} (mV vs SCE)	i_{corr} (μA/cm²)	β_c (mV/dec)	β_a (mV/dec)	CR (mpy)	%EI
Moringa leaves	Purple sweet potato						
5000	-	-506	56,80	$1,55 \times 10^{3}$	$1,02 \times 10^{-3}$	33,33	0,00
5000	1000	-477	68,10	$1,75 \times 10^{3}$	$9,97 \times 10^{-3}$	39,69	-19,89
5000	2000	-486	69,70	$1,65 \times 10^{3}$	$9,83 \times 10^{-3}$	40,61	-22,71
5000	3000	-488	70,80	$1,64 \times 10^{3}$	$1,03 \times 10^{-3}$	41,25	-24,65
5000	4000	-490	65,20	$1,53 \times 10^{3}$	$9,60 \times 10^{-3}$	38,02	-14,79
5000	5000	-492	57,10	$1,42 \times 10^{3}$	$9,05 \times 10^{-3}$	33,28	-0,53

Furthermore the value of icorr also decreases with the addition of purple sweet potato extract, with the optimum decrease observed at 3000 ppm. The decrease in corrosion rate is caused by the presence of anthocyanin compounds in purple sweet potatoes, as reported in the research of Ayende et al. [5]. In their research, Ayende et al. also found that the inhibition efficiency of purple sweet potato extract was unstable [9]. Meanwhile, anthocyanin compounds extracted from cherries have been shown to inhibit corrosion in acidic media by up to 94.44% [18].

Furthermore, purple sweet potato extract with varying concentrations was added to moringa leaves extract with a concentration of 5000 ppm. Purple sweet potato, which is rich in anthocyanins, has the ability to resist oxidation and is therefore expected to synergistically enhance inhibitor efficiency by forming a relatively dense protective film [19]. The electrochemical parameter of mixture inhibitor as shown in Table 3. The value of icorr increases with the addition of purple sweet potato extract, this results in an increased corrosion rate, causing the inhibition efficiency to decrease as the concentration of purple sweet potato extract increases. In a study conducted by Wijaya et al. [17], the addition of 2 mL of purple sweet potato extract to curcumin extract was proven to enhance inhibitor efficiency. However, the efficiency of the mixture decreased when a higher amount of purple sweet potato extract was added. A similar trend was observed with the use of purple sweet potato extract as both a standalone and mixed inhibitor in 0.2 M HCl solution, where the efficiency decreased after the concentration exceeded the optimum level [20].

3.2. Electrochemical Impedance Spectroscopy (EIS)

The Nyquist plots obtained from the EIS measurement in the absence and presence of the inhibitors are shown in Figures 2. The diameter of the semicircle on the Nyquist curve can be used as an indicator of the inhibitor's effectiveness in preventing corrosion. The larger the diameter of the semicircular arc, the greater the inhibitor's ability to protect the metal from corrosion [21, 27]. These curves do not form perfect semicircles, which can be attributed to frequency dispersion. This phenomenon is often associated with surface roughness and inhomogeneity of the electrode surface [22]. The figures show that the Nyquist plot shapes for all three inhibitors are comparable. Across all concentrations, the plots consistently display a single depressed semicircle, suggesting that the addition of inhibitors does not significantly alter the corrosion mechanism [10].

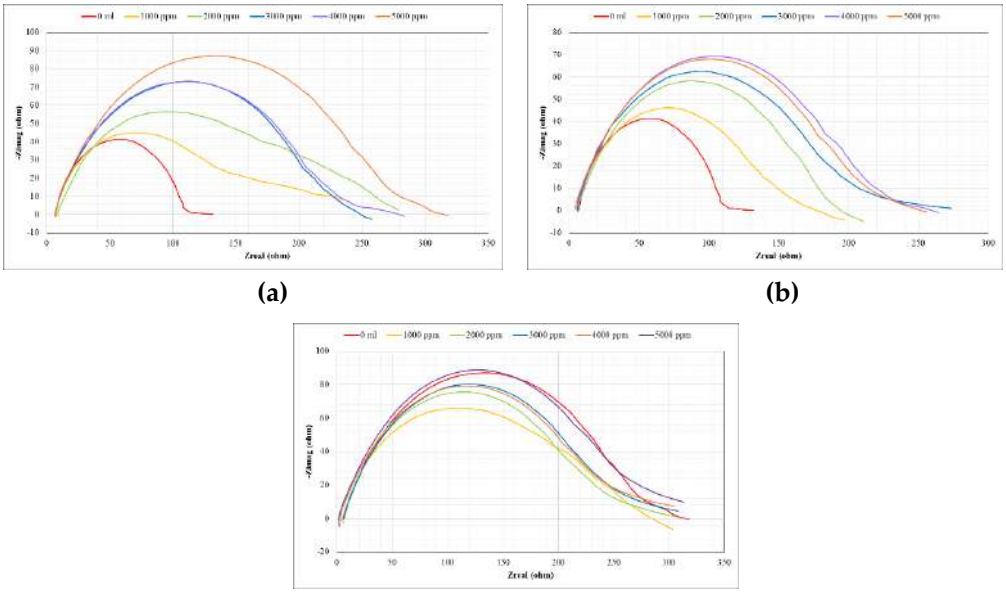

(a) **(b)**

(c)

Figure. 2. Nyquist plots in the absence and presence of inhibitor **(a)** Moringa leaves extract; **(b)** Purple sweet potato extract; **(c)** Combination of both.

Various parameters obtained from impedance measurements are given in Table 4-6. The charge transfer resistance (Rct) reflects the resistance to electron transfer at the metal surface and is inversely related to the corrosion rate [11]. To achieve a more accurate model, a constant phase element (CPE) is used in place of an ideal double-layer capacitor in the equivalent circuit (Figure 3) [12]. This element accounts for surface irregularities on the electrode, contributing to the depressed semicircle observed in Nyquist plots, as the metal–electrolyte interface behaves like a capacitor with a non-uniform surface.

Table 4 and 5 show that the value of Rct increases with the addition of moringa extract and purple sweet potato extract but not with the combination of both (Table 6). The increase in Rct values could be attributed to the formation of a protective electrochemical double layer on the metal-solution interface [13]. The proportional increase in Rct with the volume of moringa extract added indicates a rise in surface coverage, meaning a larger portion of the metal surface is being covered by the protective film. This is further supported by the increase in inhibition efficiency, which reaches up to 60.60%. For comparison, the inhibition efficiency of moringa leaves extract is slightly lower than that of neem leaf extract (69.3%), pawpaw leaf extract (68.4%), and curry leaf extract (64.6%) as reported by Chukwueze et al. [23] aslo curcuma xanthorrhiza extract that obtained 90% efficiency inhibition [28]. The inhibition efficiency, calculated from EIS results, shows the same trend as that obtained from polarization measurements.

Table 4. Impedance parameters and inhibition efficiency for API 5L in moringa leaves extract inhibitor.

C (ppm)	R_s ($\Omega.cm^2$)	R_{ct} ($\Omega.cm^2$)	CPE ($\mu S.s^n$)	n	C_{dl} ($\mu F.cm^{-2}$)	X^2	EI (%)
0	6.644	106.5	172.1	0.846	1,027.57	0.001	0
1000	7.758	147.6	180.8	0.843	1,206.56	0.214	27.85
2000	8.601	218.3	476.5	0.702	64,244.52	0.005	51.21
3000	6.450	221.2	196.8	0.768	4,958.29	0.001	51.85
4000	6.391	226	200.1	0.775	4,495.75	0.003	52.88
5000	6.374	270.3	196.2	0.762	5,866.03	0.001	60.60

Table 5. Impedance parameters and inhibition efficiency for API 5L in purple sweet potato extract inhibitor.

C (ppm)	R_s ($\Omega.cm^2$)	R_{ct} ($\Omega.cm^2$)	CPE ($\mu S.s^n$)	n	C_{dl} ($\mu F.cm^{-2}$)	X^2	EI (%)
0	6.644	106.5	172.1	0.846	1,027.57	0.001	0
1000	5.319	150.6	299.9	0.76	8,849.40	0.003	29.28
2000	6.736	169.3	302.7	0.843	2,281.07	0.125	37.09
3000	6.397	186.7	151.2	0.867	728.28	0.003	42.96
4000	5.062	216.8	350.8	0.763	11,513.65	0.173	50.88
5000	3.489	214.7	383.5	0.749	17,023.48	0.162	50.40

Table 6. Impedance parameters and inhibition efficiency for API 5L in combination of both inhibitors.

C (ppm)		R_s	R_{ct}	CPE	n	C_{dl}	X^2	EI (%)
Moringa leaves	Purple sweet potato	($\Omega.cm^2$)	($\Omega.cm^2$)	($\mu S.s^n$)		($\mu F.cm^{-2}$)		
5000	-	6.374	270.3	196.2	0.762	5,866.03	0.001	0
5000	1000	5.721	237.5	346.3	0.747	16,000.88	0.006	-13.81
5000	2000	5.397	240.9	299.2	0.766	9,118.78	0.028	-12.20
5000	3000	6.177	252.9	329.9	0.756	12,786.40	0.002	-6.88
5000	4000	2.871	247.4	316.4	0.77	9,161.61	0.018	-9.26
5000	5000	1.937	250.3	243.9	0.845	1,841.01	0.198	-7.99

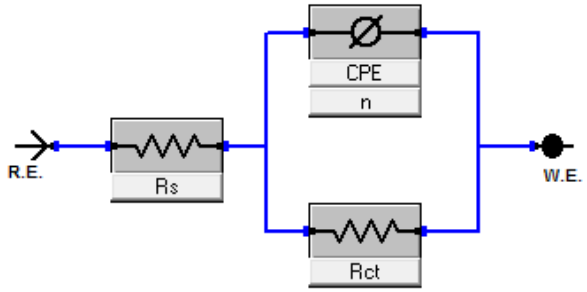

Figure. 3. The Randles circuit which is the equivalent circuit for this impedance spectra.

3.3. Fourier Transform Infrared (FTIR)

The FTIR spectrum of the moringa leaves extract, purple sweet potato extract and the combination of both are represented in Figure 4 respectively.

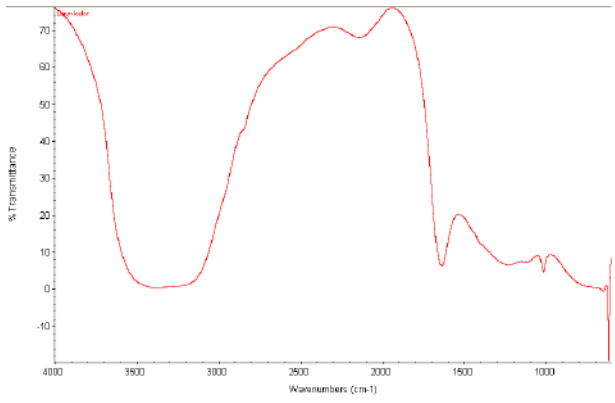

(a)

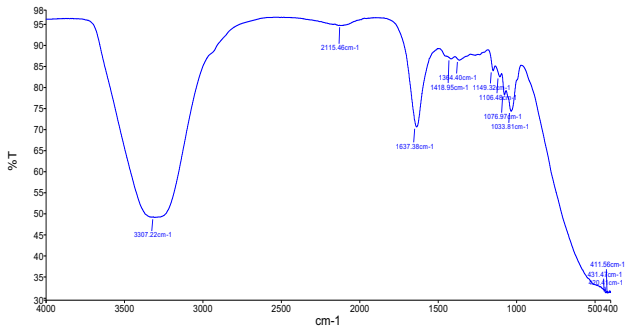

(b)

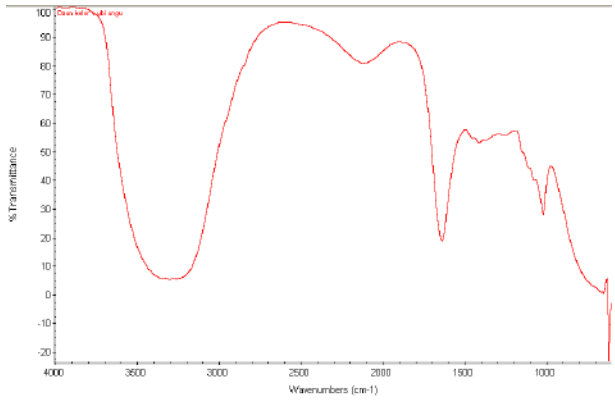

(c)

Figure. 4. Results of FTIR characterization in the absence and presence of inhibitor (a) Moringa leaves extract; (b) Purple sweet potato extract; (c) Combination of both.

FTIR is capable of revealing the distinctive characteristics of chemical bonds and molecular structures. The peaks and spectra generated by FTIR serve as unique fingerprints for identifying specific molecular structures and types of chemical bonding [24]. Figure 4(a) shows the results of FTIR characterization of moringa leaves extract solutions. A peak appears at wave number 3467 cm^{-1}, indicating O-H (COOH) acid bonds which are characteristic of alcohol and phenol compounds. Another peak at 2132 cm^{-1} indicates the presence of a C≡C bond, which is associated with alkyne compounds. Additionally, there is a spectrum peak around at 1637 cm^{-1} which indicates the C=C bond suggesting the presence of alkene compounds. Figure 4(b) shows the results of FTIR characterization of purple sweet potato extract. A peak appears at 3307.22 cm^{-1} indicating stretching O–H vibrations typical of alcohol and phenol compounds. According to Ayende et al., purple sweet potato extract contains anthocyanin components, which include OH groups [9]. Another peak at 1637.36 cm^{-1} indicates C=C vibration, , characteristic of alkene compounds. Based on these results, it can be inferred that purple sweet potato extract contains flavonoids. Figure 4(c) shows the results of FTIR characterization results for a combination of moringa extract and purple sweet potato ekstract. A peak appears at 3330 cm^{-1} indicating the presence of O-H groups from alcohol and phenol compounds. Another peak at

2120 cm^{-1} shows the presence of a C≡C bond, again associated with alkyne compounds. Additionally, a spectrum peak around 1720 cm^{-1} indicates the presence of C=C bond, suggesting alkene compounds. The FTIR analysis results reveal the presence of functional groups containing oxygen atoms and aromatic ring structures, features commonly recognized as indicators of effective corrosion inhibitors [25].

3.4. Adsorption Isotherm

The corrosion inhibition efficiency of the inhibitors on API 5L in 0.2 M HCl depends on their ability to adsorb onto the metal surface. This adsorption behavior can be quantitatively assessed through adsorption isotherm models. The coverage of moringa leaves extract and purple sweet potato extract on API 5L is defined by the following equation:

$$\theta = \frac{\eta}{100} \quad (3)$$

where η represents the inhibition efficiency of moringa leaves extract and purple sweet potato extract, as obtained from potentiodynamic polarization measurements. Several adsorption isotherm models, including Langmuir, Freundlich, Frumkin, and Temkin, have been applied to evaluate the relationship between inhibitor concentration (C) and surface coverage (θ). Among these, the adsorption behavior of the inhibitor molecules was found to best follow the Langmuir isotherm model:

$$\frac{C}{\theta} = \frac{1}{K_{ads}} + C \quad (4)$$

where Kads stands for the equilibrium constant of the adsorption process, C is the inhibitor concentration and θ represents the fraction of surface coverage. The fitting curve presented in Figure 5 exhibits a slope and correlation coefficient (R^2) that are nearly equal to 1. This slight deviation from the ideal Langmuir isotherm indicates that the adsorption layer formed by the inhibitor molecules on the metal surface is not an ideal monolayer [14].

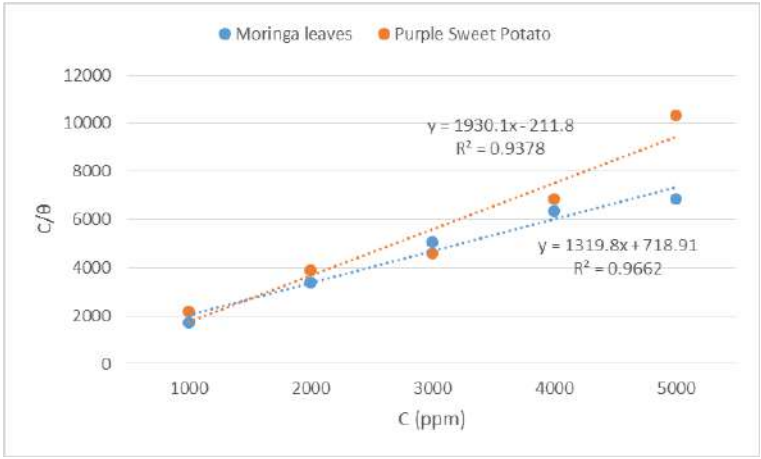

Figure. 5. Langmuir adsorption plots of moringa leaves extract and purple sweet potato extract.

The standard free energy of adsorption $\Delta G^{o}ads$ is calculated using the following equation:

$$\Delta G^{o}ads = -RT \ln (55.5\ Kads) \quad (5)$$

where R = 8.314 J/mol.K is the universal gas constant, T is the absolute temperature, and 55.5 represents the molar concentration of water. The calculated values of $\Delta G^{o}ads$ were -7.419 kJ/mol for moringa extract and -4.047 kJ/mol for purple sweet potato extract. The significantly negative values indicate strong adsorption of these compounds on the steel surface. Generally, $\Delta G^{o}ads$ values around -20 kJ/mol or less suggest electrostatic interactions between the charged metal surface and charged organic molecules in solution, while values near -40 kJ/mol or more imply charge sharing or transfer between the metal and the organic molecules [15]. For both inhibitors the values obtained are less negative than -20 kJ/mol, indicating that the adsorption onto the steel surface is primarily physical in nature [26].

3.5. Inhibition Mechanism

From several measurements that have been done, it is shown that the inhibition mechanism of moringa leaves extract inhibitor and purple sweet potato extract on API 5L steel in 0.2 M HCl is effective. FTIR results showed that the inhibitor has an -OH functional group which has properties as an antioxidant that can bind oxygen to the environment. Then, the inhibitor is adsorbed on the metal surface physically, this is shown by the value of $\Delta G^{o}ads$ being more than -20 kJ/mol and from EIS testing where the Rct value increases along with the addition of the inhibitor. The compounds of the inhibitor on the metal surface form a film layer covering the surface. Furthermore, Cl^{-} ions from HCl solution can not react with metals because of the blocking film layer, this is shown by the potentiodynamic polarization test where the corrosion rate decreases with increasing inhibitor concentration.

4. Conclusions

Moringa leaves extract and purple sweet potato extract can be used for green corrosion inhibitor, it shown from decreasing of corrosion rate and increasing of inhibition efficiency along with the addition of the inhibitor. The highest value of inhibition efficiency for moringa leaves extract and purple sweet potato extract is 73.08% and 65.31% respectively. The combination of both extract cannot be used for green corrosion inhibitor, it shown from the value of corrosion rate increase with the addition of the inhibitor. Moringa leaves extract and purple sweet potato were physically adsorbed on the steel surface.

Author Contributions: Conceptualization, Kezia; methodology, Tio Angger Pertama; software, Tio Angger Pertama; validation, Kezia, Tio Angger Pertama, Johny Wahyuadi Soedarsono and Yudha Pratesa; formal analysis, Kezia and Tio Angger Pertama; investigation, Tio Angger Pertama; resources, Kezia and Tio Angger Pertama; data curation, Tio Angger Pertama; writing—original draft preparation, Tio Angger Pertama; writing—review and editing, Kezia; visualization, Tio Angger Pertama; supervision, Johny Wahyuadi Soedarsono; project administration, Tio Angger Pertama. All authors have read and agreed to the published version of the manuscript.

Funding: This research received no external funding.

Conflicts of Interest: The authors declare no conflict of interest. The funders had no role in the design of the study; data collection, analysis, or interpretation; manuscript writing; or decision to publish the results.

References

1. D. A. Jones, Principles and Prevention of Corrosion, New York: Macmillan Publishing Company, 1992.
2. P. R. Roberge, Corrosion Engineering: Principles and Practice, McGraw Hill, 2008.
3. J. N. Kasolo, G. S. Bimenya, L. Ojok, J. Ochieng and J. W. Ogwal-Okeng, "Phytochemicals and uses of Moringa oleifera leaves in Ugandan rural communities," Journal of Medicinal Plants Research, vol. 4, pp. 753-757, 2010.
4. N. Subasree, J. Arockiaselvi, P. Kamaraj and M. Arthanareeswari, "Study of mild steel corrosion in sulphuric acid medium by moringa oleifera leaf extract by electrochemical and surface analysis studies," International journal of chemtech research, vol. 11, pp. 317-325, 2018.
5. Ayende, F. Rachmanda, J. W. Soedarsono, D. Priadi and Sulistijono, "Corrosion Behavior of API-5L in Various Green Inhibitors," Advanced Materials Research, Vols. 634-638, pp. 689-695, 2013.
6. A. Y. El-Etre and A. I. Ali, "A novel green inhibitor for C-steel corrosion in 2.0 mol•L−1 hydrochloric acid solution," Chinese Journal of Chemical Engineering, vol. 25, pp. 373-380, 2017.
7. A. A. Olajire, "Corrosion inhibition of offshore oil and gas production facilities using organic compound inhibitors - A review," Journal of Molecular Liquids, vol. 248, pp. 776-808, 2017.
8. M. F. Azmi and J. W. Soedarsono, "Study of corrosion resistrance of pipeline API 5L X42 using green inhibitor bawang dayak (Eleutherine americanna Merr.) in 1M HCl," in 2nd international Tropical Renewable Energy Conference (i-TREC), 2017.
9. Ayende, A. Rustandi, J. W. Soedarsono, D. Priadi, Sulistijono, D. N. Suprapta, G. Priyotomo and R. Bakri, "Effects of Purple Sweet Potato Extract Addition in Ascorbic Acid Inhibitor to Corrosion Rate of API 5L steel in 3.5% NaCl Environment," Applied Mechanics and Materials, vol. 709, pp. 384-389, 2014.
10. M. A. Ibraheem, A. E. A. El Sayed Fouda, M. T. Rashad and F. N. Sabbahy, "Sweet Corrosion Inhibition on API 5L Pipeline Steel," International Scholarly Research Network Metallurgy, vol. 2012, 2012.
11. M. H. Hussin and M. J. Kassim, "The corrosion inhibition and adsorption behavior of Uncaria gambir extract on mild steel in 1M HCl," Materials Chemistry and Physics, vol. 125, pp. 461-468, 2011.
12. J. R. Macdonald and W. B. Johanson, Theory in Impedance Spectroscopy, New York: John Wiley & Sons, 1987.
13. F. Bentiss, M. Traisnel and M. Lagrence, "The substituted 1,3,4-oxadiazoles: a new class of corrosion inhibitors of mild steel in acidic media," Corrosion Science, vol. 42, pp. 127-146, 2000.
14. K. Zhang, W. Yang, B. xu, Y. Chen, X. Yin, Y. Liu and H. Zuo, "Inhibitory effect of konjac glucomanan on pitting corrosion of AA5052 aluminium alloy in NaCl solution," Journal of Colloid and Interface Science, vol. 517, pp. 52-60, 2018.
15. M. Ozcan, R. Solmaz, G. Kardas and I. Dehri, "Adsorption properties of barbiturates as green corrosion inhibitors on mild steel in phosphoric acid," Colloids and Surfaces A: Physicochemical and Engineering Aspects, vol. 325, pp. 57-63, 2008.

16. A. E. S. Fouda, F. I. El Dossoki, M. F. Atia, F. M. A. E. Aziz and A. El Hossiany, "Contribution to the corrosion inhibition of aluminum by aqueous extract of Moringa oleifera in 2 M HCl," Discover Chemical Engineering, 2025.
17. A. Wijaya, J. W. Soedarsono, A. P. Laksana and T. Aditiyawarman, "Study of mixing purple sweet potato and turmeric extract as green corrosion inhibitor for API-5L in NaCl 3,5% environment," AIP Conference Proceedings, 2023.
18. Y. Teng, W. Zhang, M. Wang, C. Yu, Y. Ma, J. Bian, X. Yang and D. Zhang, "Anthocyanin as sustainable and non-toxic corrosion inhibitor for mild steel in HCl media: Electrochemical, surface morphology and theoretical investigations," Journal of Molecular Liquids, 2021.
19. Z. Zhang and X. Feng, "Synthesis and evaluation of new type plant extraction corrosion inhibitor," Geoenergy Science and Engineering, 2025.
20. Supratman, "Efektifitas ekstrak biji keluak (Pangium Edule Reinw) dan ubi ungu (Ipomoea Batatas) sebagai green corrosion inhibitor pada material baja API 5L dalam larutan 0,2M HCl (Tesis Magister)," 2019.
21. S. Prifiharni, G. Mashanafie, G. Priyotomo, A. Royani, A. Ridhova, B. Elya and J. W. Soedarsono, "Extract sarampa wood (Xylocarpus Moluccensis) as an eco-friendly corrosion inhibitor for mild steel in HCl 1M," Journal of the Indian Chemical Society, 2022.
22. M. E. Eissa, S. H. Etaiw, E. S. El-Hussieny, A. A. El Hossiany and A. E.-A. S. Fouda, "Sweet Orange Peel Extract as green sustainable corrosion inhibitor for Al in 1 M HCl," International Journal of Electrochemical Science, 2025.
23. G. N. Chukwueze, C. O. Asadu, C. E. Onu and I. S. Ike, "Evaluation of the Corrosion Inhibitive Properties of Three Different Leave Extracts on Mild Steel Iron in Sulphuric Acid Solution," Journal of Engineering Research and Reports, 2020.
24. A. B. D. Nandiyanto, R. Ragadhita and M. Fiandini, "Interpretation of Fourier Transform Infrared Spectra (FTIR): A Practical Approach in the Polymer/Plastic Thermal Decomposition," Indonesian Journal of Science & Technology, 2023.
25. I. A. Bouabdallah, F. Adjal, A. Zaabar, A. Benchikh, D. Guerniche, C. A. Ramdane-Terbouche, A. P. Piedade, M. Z. Ibrahim, N. Nasrallah and A. Abdi, "Cleome arabica L. extract as a novel green corrosion inhibitor for AISI 1045 carbon steel in 0.5 M HCl: insights from experimental and theoretical DFT analyses," RSC Advances, 2024.
26. K. H. Rashid, A. A. Khadom and S. H. Abbas, "Optimization, kinetics, and electrochemical investigations for green corrosion inhibition of low-carbon steel in 1 M HCl by a blend of onion-garlic leaves wastes," Bioresource Technology Reports, 2022.
27. A. P. S. Kaban, W. Mayangsari, M. S. Anwar, A. Maksum, R. Riastuti, T. Aditiyawarman and J. W. Soedarsono, "Experimental and modelling waste rice husk ash as a novel green corrosion inhibitor under acidic environment," Materials Today: Proceedings, 2022.
28. J. W. Soedarsono, M. N. Shihab, M. Fikri and A. Maksum, "Study of curcuma xanthorrhiza extract as green inhibitor for API 5L X42 steel in 1M HCl solution," IOP Conference Series: Earth and Environmental Science, 2018.

RiESTech
Recent in Engineering Science and Technology

MBI

Article

Comparing MLP and 1D-CNN Architectures for RUL Forecasting in Lithium Batteries

Idrus Assagaf [1,*], Agus Sukandi [1], Parulian Jannus [1], Sonki Prasetya [1], Asep Apriana [1], Ega Edistria [2], Abdul Azis Abdillah [3]

[1] Department of Mechanical Engineering, Politeknik Negeri Jakarta, Depok, Indonesia
[2] Department of Civil Engineering, Politeknik Negeri Jakarta, Depok, Indonesia
[3] The School of Engineering, University of Birmingham, Birmingham, United Kingdom
* Correspondence: idrus.assagaf@mesin.pnj.ac.id

Abstract: Accurately forecasting the Remaining Useful Life (RUL) of lithium-ion batteries is critical for optimizing battery management and ensuring operational reliability. This study compares the performance of two deep learning architectures—a Multilayer Perceptron (MLP) and a one-dimensional Convolutional Neural Network (1D-CNN)—in predicting RUL using datasets from CALCE batteries B35, B36, and B37. Data preprocessing involved outlier removal, missing value handling, and feature normalization, with key features extracted including Resistance, Constant Voltage Charging Time (CVCT), and Constant Current Charging Time (CCCT). Correlation analyses confirmed strong relationships between these features and RUL. Both models were trained and validated on preprocessed data, and their predictive accuracies were assessed using Root Mean Square Error (RMSE) and coefficient of determination (R2). Results indicated that while both architectures effectively captured battery degradation patterns, the MLP consistently outperformed the 1D-CNN, achieving on average 5% lower RMSE and 1.5% higher R2 across all tested batteries. These findings suggest that simpler fully connected networks may suffice for this forecasting task under the given feature set and preprocessing conditions. This work provides valuable insights into neural network model selection for battery health prognostics, guiding the development of efficient and accurate predictive maintenance strategies.

Keywords: Remaining Useful Life; Lithium-ion Battery; Multilayer Perceptron; One-dimensional Convolutional Neural Network; Predictive Maintenance; Battery Health Prognostics

Citation: Assagaf, I., Sukandi, A., Jannus, P., Prasetya, S., Apriana, A., Edistra, E., Abdillah, A.A. (2025). Comparing MLP and 1D-CNN Architectures for RUL Forecasting in Lithium Batteries. Recent in Engineering Science and Technology, 3(04), 49–58. Retrieved from https://www.mbi-journals.com/index.php/riestech/article/view/127

Academic Editor: Vika Rizka

Received: 5 September 2025
Accepted: 14 October 2025
Published: 31 October 2025

Publisher's Note: MBI stays neutral with regard to jurisdictional claims in published maps and institutional affiliations.

1. Introduction

The accelerating global transition toward electrified transportation and renewable energy integration is fundamentally dependent on advanced energy storage systems. Among these, lithium-ion (Li-ion) batteries have emerged as the dominant technology due to their high energy density, long cycle life, and declining costs [1], [2]. However, ensuring the safety, reliability, and longevity of these complex electrochemical systems remains a critical challenge. A battery management system (BMS) needs to predict how long a battery will last. This prediction is called Remaining Useful Life, or RUL [3]. RUL means the number of charge and discharge cycles the battery can still go through. The end of a battery's life usually happens when its capacity drops by about 20 to 30 percent from its original value.

Accurate RUL forecasting is paramount for mitigating catastrophic failures, enabling predictive maintenance, and optimizing the operational lifespan of assets. The inherent complexity of battery degradation—a nonlinear process influenced by numerous factors including operating temperature, charge/discharge rates (C-rates), and depth of discharge—makes precise prognostics a non-trivial task [4]. Traditional model-based approaches, such as those rooted in electrochemical principles or equivalent circuit models, often struggle with generalization and require intricate parameterization, limiting their practicality for real-world BMS applications [5].

In response to these limitations, data-driven methods have garnered significant attention. By leveraging historical operational data, these approaches learn the underlying degradation patterns without requiring explicit physical knowledge of the system. Machine learning (ML), and deep learning (DL) in particular, has demonstrated remarkable success in modeling complex temporal sequences for prognostics [6]. Within this domain, the Multilayer Perceptron (MLP) has been widely adopted as a foundational architecture for RUL prediction, capable of learning intricate nonlinear mappings from input features (e.g., voltage, current, temperature) to a prognostic output [7], [8].

While powerful, standard MLPs treat input data as independent and unordered vectors, potentially overlooking the critical temporal dependencies and local patterns within the sequential voltage, current, and capacity data of a charge-discharge cycle. Conversely, 1D Convolutional Neural Networks (1D-CNNs) are specifically designed to exploit sequential structure. Through their innate use of filters and pooling operations, 1D-CNNs can autonomously extract salient, hierarchical features from raw time-series data, capturing local trends and dependencies that are highly relevant for degradation modeling [9], [10]. Although 1D-CNNs have shown promise in related time-series forecasting domains, a systematic and rigorous comparison of their efficacy against the well-established MLP architecture for the specific task of Li-ion battery RUL prediction is not yet fully explored in the literature.

This study aims to address this research gap by conducting a comprehensive empirical evaluation of MLP and 1D-CNN architectures for accurate data-driven RUL forecasting. Comparing MLP and 1D-CNN provides insights on model selection for researchers seeking efficient approaches, and guides industry practitioners in adopting suitable architectures for integration into battery management systems. Utilizing publicly available benchmark datasets, we rigorously train and validate both models under identical conditions to ensure a fair comparison. Our investigation seeks to determine which architectural paradigm is better suited for capturing the complex temporal dynamics of battery degradation. The key contributions of this work are threefold:

1. To design and implement optimized MLP and 1D-CNN models for direct comparison on the task of lithium-ion battery RUL prediction.
2. To perform a quantitative and qualitative analysis of the forecasting performance of each model, evaluating metrics such as Root Mean Square Error (RMSE) and coefficient of determination (R2).

The remainder of this paper is organized as follows: Section 2 presents the Materials and Methods, including a description of the dataset, the data pre-processing procedures, and the detailed architectural configurations of the MLP and 1D-CNN models developed for this study. Section 3 provides the Results and Discussion, offering a comprehensive comparative analysis of the model performances and interpreting the findings. Finally, Section 4 concludes the paper by summarizing the key outcomes and proposing avenues for future research.

2. Research Methods

This study utilized publicly available datasets from the Center for Advanced Life Cycle Engineering (CALCE) comprising batteries B35, B36, and B37 [11]. These datasets represent lithium-ion battery cells subjected to controlled cycling tests capturing detailed electrical measurements over their lifespan until end-of-life conditions. The data includes voltage, current, resistance, and time-series information specifically relevant to battery degradation and RUL estimation. These three battery datasets were selected because they represent distinct cycling profiles, offer sufficient data granularity, and are widely utilized in benchmarking studies for RUL prediction. Other datasets were excluded due to incomplete cycles or missing key features.

The data preprocessing began with a thorough examination of the raw datasets to ensure data quality and integrity. This involved identifying and removing outliers that could adversely affect model training, followed by handling missing values through imputation or removal. The features were then normalized to ensure comparable scales across all inputs, which is critical for neural network convergence. These steps were essential to prepare the heterogeneous time-series data for effective modeling.

Following preprocessing, feature extraction focused on four key variables known to be strongly associated with battery degradation [12], [13], [14]: Resistance, Constant Voltage Charging Time (CVCT), Constant Current Charging Time (CCCT), and the RUL as the prediction target. Resistance represents the electrical resistance of the cell during operation, while CVCT and CCCT capture important aspects of the battery's charging profile, providing insight into its health status and degradation trends.

To examine the predictive relevance of these features, Pearson correlation coefficients were computed between each input feature and the RUL. This correlation analysis confirmed meaningful statistical relationships, guiding the selection of inputs for the predictive modeling phase.

Two neural network architectures were then implemented and trained for RUL forecasting: MLP and 1D-CNN. The MLP, a fully connected feedforward network, was designed to model global nonlinear relationships between the input features and RUL. In contrast, the 1D-CNN leveraged convolutional layers to capture local latent patterns in the sequential feature data. Both models underwent hyperparameter tuning and were trained using the preprocessed datasets split into training, validation, and testing subsets to ensure unbiased evaluation.

Finally, the models' performances were assessed quantitatively using RMSE and R2 on the unseen testing data. Monitoring of training and validation loss curves was conducted during training to detect convergence behavior and avoid overfitting. Visualization tools, including scatter plots of predicted versus actual RUL values, were also employed to qualitatively assess model accuracy.

This comprehensive methodology, spanning data collection, preprocessing, feature extraction, correlation analysis, model development, and performance evaluation, provided a robust framework to rigorously compare the capabilities of MLP and 1D-CNN architectures for accurate RUL forecasting in lithium-ion batteries. The pseudocode of this study can be seen in Table 1.

Table 1. Pseudocode of the main workflow for data processing, modeling, and evaluation using MLP and 1D-CNN architectures for lithium-ion battery RUL prediction.

Pseudocode
 # 1. Load and preprocess data
Load dataset from CSV file
Select features: CVCT, CCCT, resistance
Select target: RUL
Split data into training set and validation set (80/20 split)
Normalize feature data using standard scaler based on training data
 # 2. Define regression metrics function
Define function to calculate MSE, RMSE, MAE, MAPE, R2 between true and predicted values
 # 3A. MLP Model
Initialize MLP model with layers:
Dense layer with 32 units, ReLU activation, input shape = number of features
Dense layer with 16 units, ReLU activation
Dense layer with 1 unit (output)
Compile MLP model with Adam optimizer and MSE loss
Train MLP on training data for 50 epochs with batch size 16
Validate on validation data
Predict RUL on training and validation sets using trained MLP model
Calculate regression metrics for MLP predictions on training and validation data
Plot training vs validation loss and predicted vs actual values for MLP
 # 3B. 1D-CNN Model
Reshape training and validation feature data to have shape (samples, 1, features)
Initialize 1D-CNN model with layers:
Conv1D layer with 16 filters, kernel size 1, ReLU activation, input shape = (1, number of features)
Flatten layer
Dense layer with 16 units, ReLU activation
Dense layer with 1 unit (output)
Compile CNN model with Adam optimizer and MSE loss

Train CNN on reshaped training data for 50 epochs with batch size 16
Validate on reshaped validation data
Predict RUL on training and validation sets using trained CNN model
Calculate regression metrics for CNN predictions on training and validation data
Plot training vs validation loss and predicted vs actual values for CNN
 # 4. Performance summary
Create tables displaying MSE, RMSE, MAE, MAPE, R2 metrics for training and validation sets of both models
Print performance comparison

3. Results and Discussion

3.1. Modelling Results

To investigate the relationship between key battery health indicators and RUL, a correlation analysis was performed for batteries B35, B36, and B37 shown in Figure 1. The features analyzed—Resistance, CVCT, and CCCT—exhibited strong correlations with RUL across all batteries. Specifically, CVCT showed consistently strong negative correlations with RUL, ranging from -0.85 to -0.93, indicating that an increase in CVCT corresponds to a decrease in battery lifespan. Conversely, CCCT demonstrated robust positive correlations with RUL, between 0.90 and 0.92, suggesting longer CCCT is associated with longer battery life. Resistance also showed high negative correlations with RUL, between -0.87 and -0.89. These statistically significant correlations elucidate the predictive value of these features for accurate RUL forecasting in lithium-ion batteries.

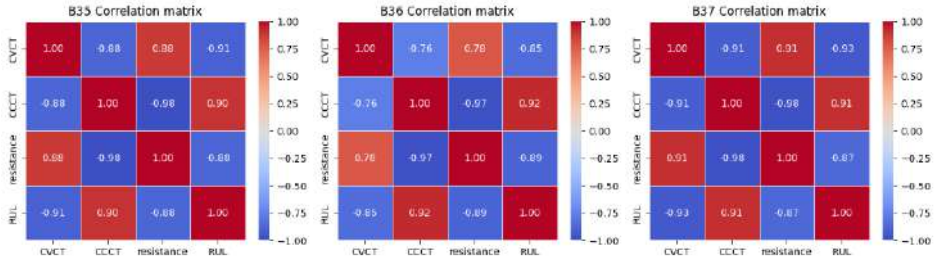

(a) (b) (c)

Figure 1. Correlation matrices illustrating the relationships among key predictive features—CVCT, CCCT, resistance—and RUL for battery cells B35, B36, and B37: **(a)** B35; **(b)** B36; (c) B37.

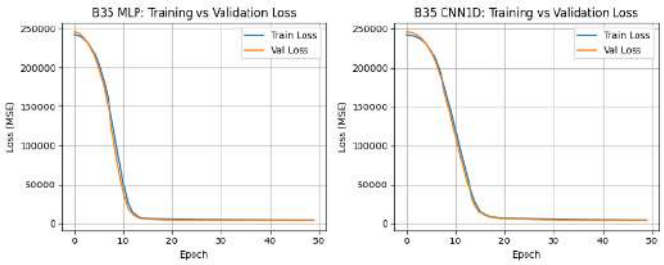

(a) (b)

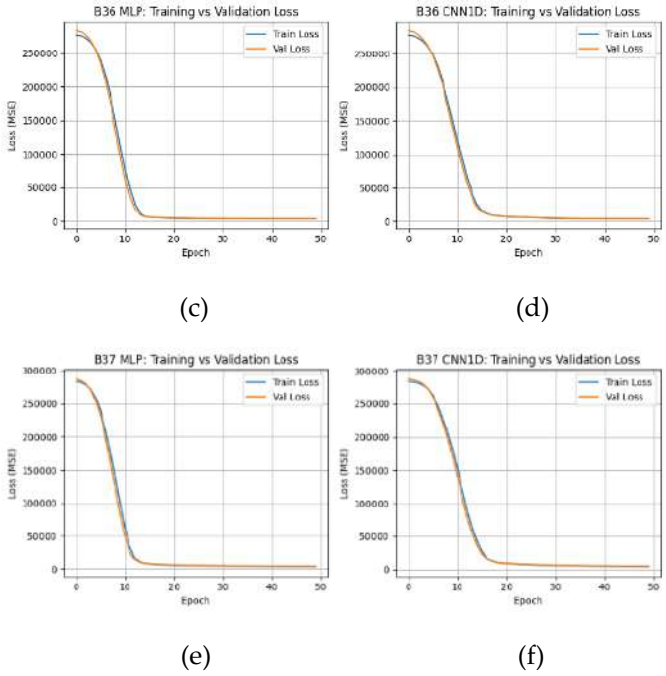

(c) (d)

(e) (f)

Figure 2. Training and validation loss curves for MLP and 1D-CNN models across battery cells B35, B36, and B37: **(a)** B35 MLP; **(b)** B35 1D-CNN; (c) B36 MLP; **(d)** B36 1D-CNN; **(e)** B37 MLP; **(f)** B37 1D-CNN.

The training performance of both MLP and 1D-CNN architectures was assessed by monitoring training and validation loss curves over epochs for each battery dataset. Across batteries B35, B36, and B37, the MLP models demonstrated rapid convergence, with both training and validation errors beginning to plateau around the 10th epoch. In contrast, the 1D-CNN models showed a slightly slower convergence pattern, with loss metrics stabilizing approximately at the 15th epoch. The early stabilization of loss values indicates effective model learning without significant overfitting, reinforcing that both architectures are capable of capturing the underlying patterns in the battery degradation data within a reasonable number of epochs. All of the training performance can be seen in Figure 2.

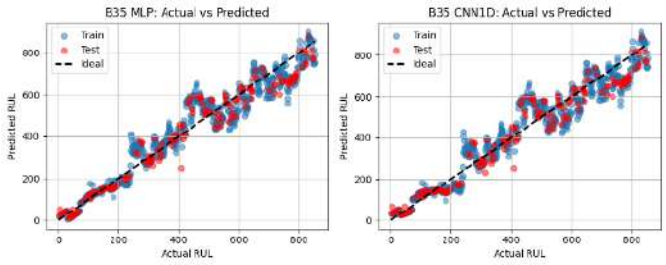

(a) (b)

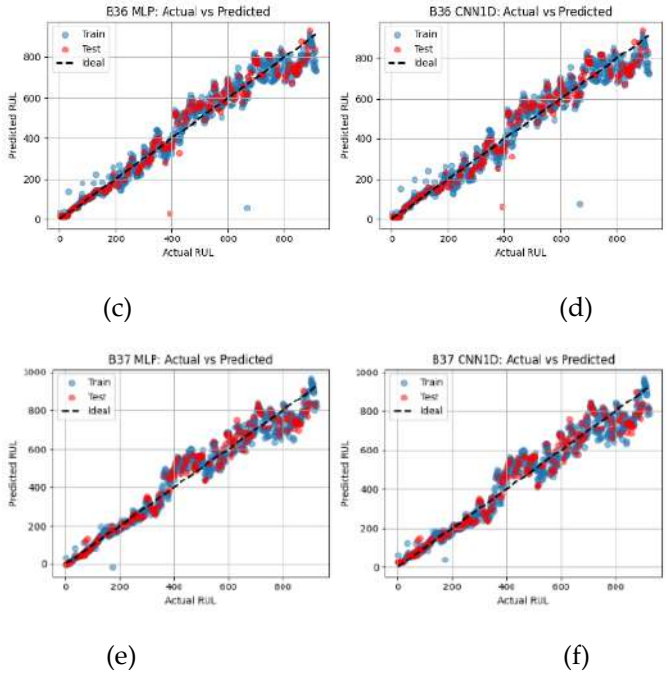

Figure 3. Scatter plots comparing predicted versus actual RUL for MLP and 1D-CNN models across battery cells B35, B36, and B37: **(a)** B35 MLP; **(b)** B35 1D-CNN; (c) B36 MLP; **(d)** B36 1D-CNN; **(e)** B37 MLP; **(f)** B37 1D-CNN.

Quantitative evaluation of the models' predictive accuracy on testing datasets was performed using RMSE and R2, key metrics for regression performance. Across all tested batteries, the MLP consistently outperformed the 1D-CNN model, evidenced by lower RMSE values and superior R^2 scores. For battery B35, the MLP achieved an RMSE of 58.19 and an R^2 of 0.945, surpassing the CNN's RMSE of 61.18 and R^2 of 0.939. Similar trends were observed for batteries B36 and B37, with MLP models attaining RMSEs of 60.97 and 59.55 and R^2 values of 0.945 and 0.949 respectively, compared to the CNN's relatively higher error rates and marginally lower explanatory power. Visualization through scatter plots (Figure 3) comparing predicted versus actual RUL further substantiated these findings, where predictions from MLP models showed tighter clustering along the ideal diagonal line, reflecting more precise predictions.

Collectively, these results validate the superior efficacy of the MLP architecture for RUL forecasting in lithium-ion batteries under the current experimental conditions, while also demonstrating that the 1D-CNN remains a competent alternative. This comprehensive analysis of correlation, training dynamics, and prediction accuracy provides strong evidence supporting the feature selection and modeling approaches adopted in this study.

3.2. Discussion

This study aimed to compare the capabilities of MLP and 1D-CNN architectures for forecasting the RUL of lithium-ion batteries, leveraging key feature correlations and predictive performance metrics. The discussion here interprets the implications of the results, contextualizes them within existing literature, and outlines the significance and limitations of the work.

The strong correlations observed between CVCT, CCCT, Resistance, and RUL corroborate prior findings that these electrical characteristics serve as reliable indicators of battery degradation and health status. These statistically significant correlations reinforce the relevance of these features in RUL estimation models and align with earlier studies that highlight the critical role of charging behaviors and resistance changes in battery aging processes.

From a modeling perspective, both architectures demonstrated effective learning as evidenced by the stable convergence of training and validation losses. The MLP's quicker convergence suggests it may efficiently capture the underlying feature patterns with fewer training iterations, potentially providing computational advantages. Meanwhile, the 1D-CNN, designed to extract features through convolutional operations, achieved competitive but slightly less optimal predictive performance. In this study, the MLP exhibited superior results compared to the 1D-CNN for the specific feature set and data preprocessing applied, indicating that fully connected architectures like MLP may be more suited for RUL prediction under these conditions.

Predictive accuracy metrics, particularly RMSE and R2, consistently favored the MLP across multiple battery datasets. The modest yet consistent better performance of MLP models suggests that fully connected architectures can better generalize the nonlinear relationships between the selected input features and RUL in this context. These results extend existing literature by providing a direct comparative analysis, highlighting that simpler architectures like MLP should not be discounted in favor of more complex models without empirical justification.

Nevertheless, some limitations should be acknowledged. The present study is limited by a relatively small dataset size (only three batteries) and experiments conducted in controlled laboratory settings. These constraints affect the generalizability of findings to batteries operated in varied real-world environments, indicating the need for future research with larger, more diverse datasets and field conditions.

4. Conclusions

This study systematically compared the performance of MLP and 1D-CNN architectures for forecasting the RUL of lithium-ion batteries using features extracted from battery cycling data. The empirical results demonstrated that both approaches can effectively model battery degradation trajectories, leveraging key health indicators such as Capacity, Resistance, CVCT, and CCCT. However, the MLP model consistently outperformed the 1D-CNN in capturing the temporal dependencies and subtle feature variations inherent in the degradation process, resulting in superior accuracy and robustness in RUL predictions.

Additionally, feature engineering and the inclusion of statistical time-series descriptors contributed significantly to improving model performance across architectures. While the CNN's convolutional layers are adept at extracting localized temporal patterns useful for prognostics, MLP's fully connected layers proved more efficient for capturing the global nonlinear relationships present in the selected features.

This research highlights the importance of selecting architecture types aligned with the nature of prognostic data. The MLP model's effectiveness in interpreting battery health signals supports its practical application for predictive maintenance in electric vehicle battery management systems. Future work should focus on integrating sensor fusion and extending the approach to real-time RUL estimation under diverse operational conditions, further enhancing reliability and lifespan optimization. In summary, the findings advocate for the deployment of MLP architectures over 1D-CNN to achieve more accurate and reliable RUL forecasting in lithium battery systems.

Supplementary Materials: The Calce (public) dataset can be downloaded at: https://calce.umd.edu/battery-data.

Author Contributions: "Conceptualization, methodology, writing, review and editing I.A.; Data Collection, validation, writing, review and editing A.S., A.A., P.J., S.P.; Software, Programming, Data Visualization and Data Analysis, E.E., A.A.

Funding: This research was funded by Politeknik Negeri Jakarta, grant number XXX.

Acknowledgments: The authors would like to express their sincere gratitude to Politeknik Negeri Jakarta for providing the funding that made this research possible. This financial support was instrumental in facilitating the study and the successful completion of this work.

Conflicts of Interest: The authors declare no conflict of interest.

References

1. T. Feng *et al.*, "Energy transition in the new era: The impact of renewable electric power on the life cycle assessment of automotive power batteries," *Renew Energy*, vol. 236, p. 121365, Dec. 2024, doi: 10.1016/J.RENENE.2024.121365.
2. B.-H. ; Jiang *et al.*, "A Review of Modern Electric Vehicle Innovations for Energy Transition," *Energies 2024, Vol. 17, Page 2906*, vol. 17, no. 12, p. 2906, Jun. 2024, doi: 10.3390/EN17122906.
3. G. Krishna *et al.*, "Advanced battery management system enhancement using IoT and ML for predicting remaining useful life in Li-ion batteries," *Sci Rep*, vol. 14, no. 1, pp. 1–18, Dec. 2024, doi: 10.1038/S41598-024-80719-1;SUBJMETA=117,166,639,705,987;KWRD=COMPUTER+SCIENCE,ELECTRICAL+AND+ELECTRONIC+ENGINEERING.
4. K. Das and R. Kumar, "Electric vehicle battery capacity degradation and health estimation using machine-learning techniques: a review," *Clean Energy*, vol. 7, no. 6, pp. 1268–1281, Dec. 2023, doi: 10.1093/CE/ZKAD054.
5. N. Bhushan, S. Mekhilef, K. S. Tey, M. Shaaban, M. Seyedmahmoudian, and A. Stojcevski, "Overview of Model- and Non-Model-Based Online Battery Management Systems for Electric Vehicle Applications: A Comprehensive Review of Experimental and Simulation Studies," *Sustainability 2022, Vol. 14, Page 15912*, vol. 14, no. 23, p. 15912, Nov. 2022, doi: 10.3390/SU142315912.
6. A. A. Abdillah, H. Sun, H. Xu, and Q. Zhou, "State of Health Prediction for Lithium-Ion Batteries Using Partial Charging-Transformer-Based Deep Learning Models," in *Proceedings of the 11th World Congress on Mechanical, Chemical, and Material Engineering (MCM'25)*, 2025.

7. A. A. Abdillah, C. Zhang, Z. Ren, J. Li, H. Xu, and Q. Zhou, "Data-driven modelling of battery state-of-health using multi-criteria-based feature reduction," *Int. J. Powertrains*, vol. 14, no. 2, pp. 143–160, 2025.
8. A. A. Abdillah, C. Zhang, Z. Sun, J. Li, H. Xu, and Q. Zhou, "Data-driven Modelling for EV Battery State of Health Estimation using SFS-PCA Learning," *Proceedings of the 2023 7th CAA International Conference on Vehicular Control and Intelligence, CVCI 2023*, 2023, doi: 10.1109/CVCI59596.2023.10397248.
9. K. Ucar, "Improving electric vehicle state of charge estimation with wavelet transform-integrated 1D-CNN pooling layers," *J Energy Storage*, vol. 117, p. 116202, May 2025, doi: 10.1016/J.EST.2025.116202.
10. J. Mou, Q. Yang, Y. Tang, Y. Liu, J. Li, and C. Yu, "Prediction of the Remaining Useful Life of Lithium-Ion Batteries Based on the 1D CNN-BLSTM Neural Network," *Batteries 2024, Vol. 10, Page 152*, vol. 10, no. 5, p. 152, Apr. 2024, doi: 10.3390/BATTERIES10050152.
11. "Battery Data | Center for Advanced Life Cycle Engineering." Accessed: Sep. 03, 2025. [Online]. Available: https://calce.umd.edu/battery-data
12. W. ; Zhou, Q. ; Lu, Y. Zheng, W. Zhou, Q. Lu, and Y. Zheng, "Review on the Selection of Health Indicator for Lithium Ion Batteries," *Machines 2022, Vol. 10, Page 512*, vol. 10, no. 7, p. 512, Jun. 2022, doi: 10.3390/MACHINES10070512.
13. M. Li *et al.*, "State of Health Estimation and Battery Management: A Review of Health Indicators, Models and Machine Learning," *Materials 2025, Vol. 18, Page 145*, vol. 18, no. 1, p. 145, Jan. 2025, doi: 10.3390/MA18010145.
14. D. Liu, J. Zhou, H. Liao, Y. Peng, and X. Peng, "A health indicator extraction and optimization framework for lithium-ion battery degradation modeling and prognostics," *IEEE Trans Syst Man Cybern Syst*, vol. 45, no. 6, pp. 915–928, Jun. 2015, doi: 10.1109/TSMC.2015.2389757.

PT. Mencerdaskan Bangsa Indonesia

PT MENCERDASKAN BANGSA INDONESIA
(MBI), 4th Floor Gedung STC Senayan Room
31-34, Jl. Asia Afrika Pintu IX, Jakarta 10270,
Indonesia.